



The GeMS/GSAOI Galactic Globular Cluster Survey (G4CS). I. A Pilot Study of the Stellar Populations in NGC 2298 and NGC 3201

Stephanie Monty^{1,2} , Thomas H. Puzia³ , Bryan W. Miller⁴ , Eleazar R. Carrasco⁴ , Mirko Simunovic^{5,14} ,
Mischa Schirmer^{4,6} , Peter B. Stetson⁷ , Santi Cassisi⁸ , Kim A. Venn¹ , Aaron Dotter⁹ , Paul Goudfrooij¹⁰ ,
Sibilla Perina¹¹, Peter Pessev¹² , Ata Sarajedini¹³, and Matthew A. Taylor^{5,14}

¹ Department of Physics and Astronomy, University of Victoria, Victoria, BC V8W 3P2, Canada; montys@uvic.ca

² Research School of Astronomy and Astrophysics, Australian National University, Canberra, ACT 2611, Australia

³ Institute of Astrophysics, Pontificia Universidad Católica de Chile, Av. Vicuña Mackenna 4860, 782-0436 Macul, Santiago, Chile; tpuzia@astro.puc.cl

⁴ Gemini Observatory/AURA, Southern Operations Center, Casilla 603, La Serena, Chile

⁵ Gemini Observatory, 670 North A'ohoku Place, Hilo, HI 96720, USA

⁶ Max-Planck-Institut für Astronomie, Königstuhl 17, D-69117 Heidelberg, Germany

⁷ Herzberg Astronomy and Astrophysics, National Research Council Canada, Victoria, BC V9E 2E7, Canada

⁸ INAF—Astronomical Observatory of Abruzzo, Via M. Maggini, I-64100 Teramo, Italy

⁹ Harvard-Smithsonian Center for Astrophysics, Cambridge, MA 02138, USA

¹⁰ Space Telescope Science Institute, 3700 San Martin Drive, Baltimore, MD 21218, USA

¹¹ INAF—Astronomical Observatory of Torino, Via Osservatorio 20, I-10025 Pino Torinese, Italy

¹² Gran Telescopio Canarias, Instituto de Astrofísica de Canarias, Universidad de La Laguna, Spain

¹³ Department of Astronomy, University of Florida, 211 Bryant Space Science Center Gainesville, FL 32611, USA

Received 2017 November 30; revised 2018 July 31; accepted 2018 August 15; published 2018 October 4

Abstract

We present the first results from the GeMS/GSAOI Galactic Globular Cluster Survey (G4CS) of the Milky Way globular clusters NGC 3201 and NGC 2298. Using the Gemini South Adaptive Optics Imager (GSAOI), in tandem with the Gemini Multi-conjugate adaptive optics System (GeMS) on the 8.1 m Gemini-South telescope, we collected deep near-IR observations of both clusters, resolving their constituent stellar populations down to $K_s \simeq 21$ Vega mag. Point-spread function (PSF) photometry was performed on the data using spatially variable PSFs to generate JHK_s photometric catalogs for both clusters. These catalogs were combined with *Hubble Space Telescope* (*HST*) data to augment the photometric wavelength coverage, yielding catalogs that span the near-UV to near-IR. We then applied 0.14 mas yr^{-1} accurate proper-motion cleaning and differential-reddening corrections and chose to anchor our isochrones using the lower main-sequence knee and the main-sequence turnoff prior to age determination. As a result of the data quality, we found that the K_s versus $F606W - K_s$ and $F336W$ versus $F336W - K_s$ color–magnitude diagrams were the most diagnostically powerful. We used these two color combinations to derive the stellar population ages, distances, and reddening values for both clusters. Following isochrone fitting using three different isochrone sets, we derived best-fit absolute ages of 12.2 ± 0.5 Gyr and 13.2 ± 0.4 Gyr for NGC 3201 and NGC 2298, respectively. This was done using a weighted average over the two aforementioned color combinations, following a pseudo- χ^2 determination of the best-fit isochrone set. Our derived parameters are in good agreement with recent age determinations of the two clusters, with our constraints on the ages being or ranking among the most statistically robust.

Key words: galaxies: star clusters: general – globular clusters: individual (NGC 2298, NGC 3201) – infrared: stars – instrumentation: adaptive optics – stars: low-mass – ultraviolet: stars

1. Introduction

1.1. Complexity of GC Stellar Populations

The study of resolved globular clusters (GCs) provides unique leverage on some of the most pressing questions in astronomy, ranging from our understanding of stellar structure and evolution, to the details of star formation and chemical enrichment processes, to the formation histories of galaxies and the beginnings of structure formation in the universe (e.g., Gratton et al. 2004; Renzini 2013, 2017; Kruijssen 2014; Vanzella et al. 2017, and references therein). The *Hubble Space Telescope* UV Legacy Survey of Galactic Globular Clusters (Piotto et al. 2015) and the *Hubble Space Telescope* ACS Survey of Galactic Globular Clusters (Sarajedini et al. 2007) obtained deep near-UV¹⁵ and optical¹⁶ photometry for about

60 Milky Way (MW) GCs, enabling the creation of high-quality panchromatic color–magnitude diagrams (CMDs). Analogous to the theoretical stellar-evolution-tracing Hertzsprung–Russell diagrams, deep CMDs can be used to test theories of stellar evolution and star cluster formation. Individual GCs constitute the best available approximations to simple stellar populations, being composed of coeval stars with virtually the same chemical composition. As such, they frequently serve as calibrators for stellar population synthesis models, which can then be used to study distant, unresolved stellar systems. The deep CMDs that arose from the *Hubble Space Telescope* (*HST*) surveys have produced a range of important benchmark measurements and several unexpected findings. For instance, it was found that a number of Galactic GCs harbor multiple stellar populations (e.g., Milone et al. 2008; Piotto et al. 2015), a result with far-reaching consequences for our understanding of their formation (e.g., Renzini et al. 2015) and with close ties to star formation physics. The second prominent result was the determination of GC relative

¹⁴ Gemini Science Fellow.

¹⁵ F275W[UV] and F336W[U] WFC3 filters.

¹⁶ F438W[B] WFC3 and F606W[V] and F814W[I] ACS filters.

ages with sufficient precision to directly probe the formation and evolution of the galactic halo (e.g., Marín-Franch et al. 2009; Dotter et al. 2010, 2011; Leaman et al. 2013). These results suggest stark differences between the early formation history of the inner and outer halo, providing further evidence that the evolution of the outer halo involved the disruption and accretion of dwarf satellite galaxies (e.g., Searle & Zinn 1978; Freeman & Bland-Hawthorn 2002; Helmi 2008; Ivezić et al. 2012).

1.2. The Role of Near-infrared Observations

Near-IR CMDs offer significant advantages when compared to pure UV–optical CMDs, such as the following: (i) near-IR colors are much less affected by differential reddening (DR) than optical colors, and (ii) near-IR isochrones exhibit a very characteristic S-shaped main sequence (MS) that can be used for accurate, *absolute* age determinations. This characteristic shape is attributed to low-mass MS stars, which show a well-defined (faintward) bending, due to collision-induced and roto-translational absorption of hydrogen molecules (H_2 – H_2 and other molecular pairs, such as H_2 –He, H_2 – CH_4 , etc.) at near-IR wavelengths (also referred to as the MS “knee” or MSK; Borysow et al. 2001; Borysow 2002; Gustafsson et al. 2009; Frommhold et al. 2010; Richard et al. 2012). The resultant difference in color and luminosity between the MS turnoff (MSTO) point and the lower MSK depends predominantly on metallicity, while the luminosity and color of the MSK are virtually independent of age at any given metallicity (Calamida et al. 2009). Additionally, because the convective motions in the stellar atmospheres are mostly adiabatic at low stellar masses (Saumon & Marley 2008), the MSK is anchored in a regime of well-understood stellar structure and evolution. Therefore, by exploiting the metallicity-dependence-dominated MSTO–MSK distance, the age independence of the MSK at fixed metallicity, and its well-understood physics, the observed MSTO–MSK color and luminosity difference form a robust *absolute* theoretical reference frame that allows for the measurement of absolute GC ages with uncertainties of about 1 Gyr. This remarkable property of near-IR CMDs was recently exploited by Massari et al. (2016), Correnti et al. (2016), and Saracino et al. (2016) using various isochrone-fitting techniques. Finally, because near-IR CMDs contain the two aforementioned MS reference points, i.e., the MSTO and MSK, the age information extracted from their analysis becomes independent of cluster distance and screen-type reddening effects.

1.3. The GeMS/GSAOI Galactic Globular Cluster Survey

In this paper we describe the first results from the GeMS/GSAOI Galactic Globular Cluster Survey (G4CS). The G4CS is conducting a homogeneous, deep near-IR CMD study of MW GCs covering a broad spectral energy distribution (SED) baseline in order to (i) investigate the morphology of near-IR CMDs, particularly at low stellar masses; (ii) determine the internal consistency and calibration of model CMD predictions for various near-IR+optical+near-UV filter combinations, thereby testing the influence of variations in the molecular absorption bands on isochrones using information from publicly available high-resolution spectroscopy (e.g., Carretta et al. 2009, 2010); (iii) derive absolute GC ages with accuracies of about 1 Gyr; and (iv) quantify and characterize binary fractions and blue straggler star populations.

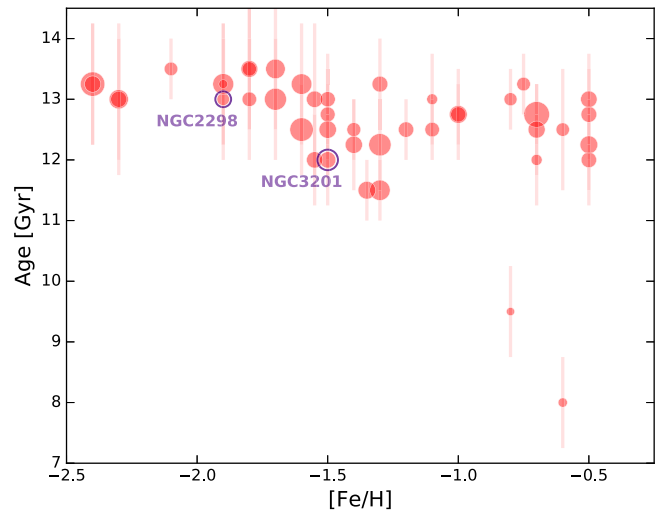


Figure 1. Age–metallicity relationship for our full G4CS target sample with available data from Dotter et al. (2010). The two GCs from this study are circled and correspondingly labeled. The symbol size scales with the V-band integrated luminosity; larger symbols correspond to brighter GCs. Note that the whole sample covers the transition region between the flat and steep age–metallicity relation. Utilizing our excellent age/metallicity resolution, we aim to clearly resolve the transition between these two GC subpopulations.

The G4CS target list was compiled through selecting GCs included in the recent *HST* surveys of Galactic GCs, to ensure that deep near-UV+optical photometry is available (Sarajedini et al. 2007; Piotto et al. 2015), with the additional restriction that the GCs lay no further than 23 kpc to ensure that the MSK can be detected in a reasonable amount of time with GeMS/GSAOI at the 8.1 m Gemini-South telescope. In order to study as broad a parameter space as possible, the target sample covers a range in GC ages ($t \simeq 8.0$ – 13.5 Gyr), metallicities ($[Z/H] \simeq -2.37$ to -0.32 dex), and masses ($M_{GC} \simeq 10^{3.75}$ – $10^{6.05} M_{\odot}$; see also Figure 1).

This paper presents the results for the first two GCs observed from the sample: NGC 2298 and NGC 3201. These two GCs were selected, in part, as a result of little indication of multiple stellar populations in their near-UV/optical CMDs (Piotto et al. 2015), making them two of the few GCs that may most closely resemble simple stellar populations. Both clusters have horizontal branches that could be influenced by the “second parameter” effect, and NGC 3201 may be about a gigayear younger than the oldest GCs (Milone et al. 2014). This implies that NGC 3201 is a candidate for having been formed in a dwarf galaxy and later accreted into the MW halo (Mackey & Gilmore 2004). Indeed, evidence of extratidal stars has been found around both clusters (Balbinot et al. 2011; Anguiano et al. 2016). Both clusters also experience relatively high reddening ($E_{B-V} \simeq 0.2$ mag), making it advantageous to study them in the near-IR. Additionally, NGC 3201 may be considered a control cluster since it has been used by both Calamida et al. (2009) and Bono et al. (2010) to demonstrate the MSTO–MSK method using VLT MAD and *HST*, respectively. Therefore, being able to compare our analysis to these earlier results will allow us to test the efficacy of our methods. The properties of the two GCs studied thus far are presented in Table 1.

This paper is organized as follows: The observations and data reduction are presented in Section 2. In Section 3 we describe the various experiments undertaken to obtain the best

Table 1
Fundamental GC Parameters

Parameter	NGC 3201	NGC 2298
Distance (kpc)	4.9	10.8
$(m - M)_V$	14.2	15.6
E_{B-V}	0.24	0.14
r_h (pc)	4.4	3.1
M_V	-7.45	-6.31
[Fe/H]	-1.59	-1.92

Note. All values are taken from the MW GC McMaster Catalog (Harris 1996; 2010 Edition). Note that the distance moduli and absolute magnitudes are not corrected for reddening, while the distance has been corrected.

point-spread function (PSF) photometry given the characteristics of our observations and describe the zero-point calibration, proper-motion (PM) cleaning, and DR corrections. Section 4 describes our methodology and results of isochrone fitting. Finally, Section 5 concludes with a summary of the work.

2. Observations and Data Reduction

2.1. NGC 3201 and NGC 2298 Data Acquisition

The observations were conducted using the Gemini South Adaptive Optics Imager (GSAOI; for details see McGregor et al. 2004; Carrasco et al. 2012). GSAOI is fed by the Gemini Multi-conjugate adaptive optics System (GeMS; Neichel et al. 2014a, 2014b; Rigaut et al. 2014), a facility adaptive optics (AO) system mounted on the Gemini-South telescope located on Cerro Pachón in Chile. GeMS uses five laser guide stars (LGSs) to correct for atmospheric distortion and up to three natural guide stars (NGSs) brighter than $R = 15.5$ mag to compensate for tip-tilt and plate scale variations over the $2'$ -diameter field of view (FOV) of the AO bench unit (CANOPUS; Rigaut et al. 2014). GSAOI is a near-IR AO camera and companion instrument to GeMS, which receives and images the corrected near-IR light output from GeMS. Together they deliver near-diffraction-limited images in the wavelength interval of 0.9–2.4 μm . The GSAOI focal plane consists of a 2×2 mosaic of Rockwell HAWAII-2RG 2048 \times 2048 detector arrays and provides an FOV of 85×85 arcsec² on the sky with a scale of $0''.02$ pixel⁻¹ and gaps of $\sim 2''.5$ between arrays.

The central regions of the two target Galactic GCs, NGC 3201 and NGC 2298, were imaged through the z , J , H , and K_s standard GSAOI filters.¹⁷ Figure 2 shows the area covered by our GeMS/GSAOI observations for NGC 3201 (left panel) and NGC 2298 (right panel) GCs overlaid on top of *HST*/WFC3 near-UV+optical stacked images from Soto et al. (2017). All images were acquired in photometric conditions and with a variable natural seeing.

The observational strategy consisted of obtaining deep images in all four bands to cover a wide near-IR SED baseline and to study the CMD morphology down to the MSK. This strategy allowed us to reach faint magnitudes (see Section 3), while sacrificing the bright end of the luminosity function, as all stars brighter than $K_s \simeq 12$ mag were saturated. Nine 30 s exposures were obtained for each GC in each filter, using an

offset of $5''$ between individual exposures, following a 3×3 dither pattern to fill the gaps between the arrays. A few subexposures suffered from the effect of the variable seeing present during the observations, reducing the effective exposure time in some filters. This was the case for NGC 3201, where one exposure from both the J and H filters had to be removed from the data set. The entire data set obtained with the z filter, for both GCs, was unusable owing to poor image quality (the average AO-corrected FWHM of the stellar PSF was larger than $0''.3$). Therefore, the z -band data sets are not considered in the subsequent analysis. Table 2 summarizes the values of natural seeing measured by the differential image motion monitor at Cerro Pachón, the total exposure time, the average airmass of the observations, the average resolution derived from stars over the field (AO-corrected FWHM), and the average Strehl ratios estimated from the observations for the two GCs.

2.2. Laser Guide Star Wave Front Sensor Misalignment Problem

The PSFs of the stars are uncharacteristically elongated and distorted in both data sets. The PSF distortions are more pronounced at the edges of the images, and they are much larger than the variations expected in typical multi-conjugate adaptive optics (MCAO) images. In typical GeMS/GSAOI images the PSF is more or less uniform across the GSAOI FOV, with a variation at the level of 8%–20% (e.g., Neichel et al. 2014a, 2014b; Rigaut et al. 2014; Dalessandro et al. 2016). The amount of variation depends on the selected NGS constellation, the number of NGSs used, the observing conditions (mainly seeing), the laser photon return, and other parameters (Neichel et al. 2014b; Rigaut et al. 2014). Even for fields where only one NGS is available, the PSF is fairly uniform across the GSAOI FOV (see Schirmer et al. 2015). The source of the distortions detected in the images was traced to a temporary misalignment in the laser guide star wave front sensor (LGSWFS) located inside the AO bench unit CANOPUS.¹⁸ The LGSWFS misalignment introduced additional distortions to the PSF, affecting the PSF performance of all the GeMS/GSAOI images observed between 2013 November and 2014 June, during which the data for our two GCs were collected. The NGC 3201 data set suffered more from the LGSWFS misalignment than the NGC 2298 data set, as the NGC 2298 data were collected after the implementation of a software fix for the misalignment during the 2014 February observing block. The extent of the effect of the LGSWFS misalignment is highlighted in the insets of Figure 3, showing the K_s -band GeMS/GSAOI co-added mosaic images of NGC 3201 (top) and NGC 2298 (bottom). The insets in Figure 3 correspond to a region located inside array 2, the array associated with the worst degradation of the PSF, with a sample of the worst and best PSFs given (top and bottom insets for NGC 3201 and NGC 2298, respectively). In the NGC 2298 data set the PSF is more uniform across the FOV and the shape is less affected by the LGSWFS misalignment, while in NGC 3201 the shape of the PSF is more variable across the FOV and the objects show elongations that mimic a “mouse-ear” form. Figure 4 shows the FWHM and ellipticity variations across

¹⁷ Filter transmission curves are available at <http://www.gemini.edu/sciops/instruments/gsaoi/instrument-description/filters>.

¹⁸ The report with the detailed discussion about technical aspects of the LGSWFS misalignment problem and subsequent solution (www.gemini.edu/sciops/instruments/gems/introduction-gems/canopus) is available upon specific request from the Gemini Observatory staff.

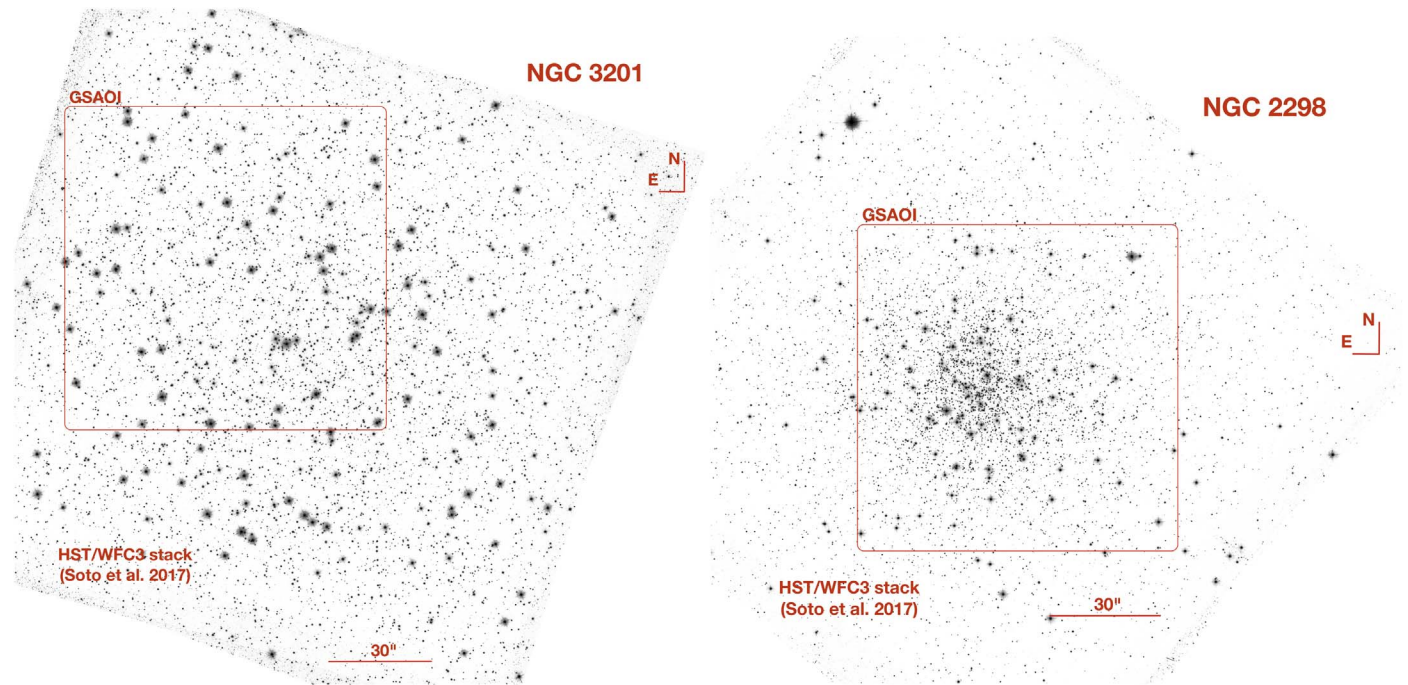


Figure 2. *HST*/WFC3 stacked UV+optical (F275W+F336W+F438W) grayscale images of NGC 3201 (left) and NGC 2298 (right) from Soto et al. (2017). The red squares represent the area covered by our GeMS/GSAOI observations.

Table 2
Observing Log

Cluster	Filter	Exp. Time (s)	Airmass	Natural Seeing	AO FWHM	Strehl (%)
NGC 3201	<i>J</i>	8 × 30	1.062		0".14	3
	<i>H</i>	8 × 30	1.073	0".72	0".12	8
	<i>K_s</i>	9 × 30	1.085		0".11	15
NGC 2298	<i>J</i>	9 × 30	1.124		0".10	6
	<i>H</i>	9 × 30	1.149	0".83	0".08	10
	<i>K_s</i>	9 × 30	1.177		0".08	24

Note. NGC 3201 and NGC 2298 were observed during the nights of 2014 January 12–13 (program ID: GS-2013B-Q-61) and 2014 February 12–13 (program ID: GS-2014A-Q-13), respectively.

the observed fields in both GCs. In this figure one can see the effect of the LGSWFS misalignment along the edges of the four arrays, particularly, as mentioned, in the upper left-hand corner of array 2 for NGC 3201. The solution developed during the course of this analysis to compensate for the image degradation is presented in Section 3.

2.3. Data Reduction

The data were reduced using the THELI software package (Erben et al. 2005; Schirmer 2013) following standard near-IR data reduction steps, beginning with the application of a nonlinearity correction to all raw images. Flat-field calibrations were performed using lamp-on (bright) and lamp-off (dark) dome flats, in order to create median-combined, master, dark, and bright flats. The master dark flat was then subtracted from the master bright flat, after which the resulting frame was normalized to unity. Science frames were then subsequently

flat-fielded and the gain differences between different arrays adjusted based on the master flats. The background in each filter was then constructed from the dithered science frames (eight to nine images depending on the object and filter used) using a two-pass background model according to the following recipe: (i) The flat-fielded science exposures were combined by their median without any masking, to remove the bulk of the sky signal. (ii) SExtractor (Bertin & Arnouts 1996) was run to identify and mask all objects with a detection threshold of 1.5σ above the sky and with a minimum area of 5 pixels. To minimize the effect of fainter halos and avoid dark halos in the final co-added images, the isophotal ellipses for masking were enlarged using a mask expansion factor between 6 and 10, minimizing the dark halo effect in the co-added images and in the photometric precision (see Schirmer et al. 2015, for a discussion). (iii) The resulting background models were then rescaled to match individual background levels of the original images and then subtracted.

The astrometric calibration and distortion correction were then derived using the program SCAMP (Bertin 2006) within THELI. We constructed the reference catalog from archival *HST*/ACS F814W (*I*-band) images, as these images have precise astrometric and distortion corrections and fully overlap with the GSAOI fields of NGC 3201 and NGC 2298 (see Figure 2). For each GC, a common astrometric solution was then derived to ensure that all filters were resampled using common WCS and pixel positions. Prior to creating the mosaic science frames, sky-background subtraction was performed on individual images to homogenize the zero background level across the four GSAOI arrays. The resulting images were then co-added using the application SWarp (Bertin 2010) within THELI. Figure 3 shows the *K_s*-band final co-added images for NGC 3201 (top panel) and NGC 2298 (bottom panel).

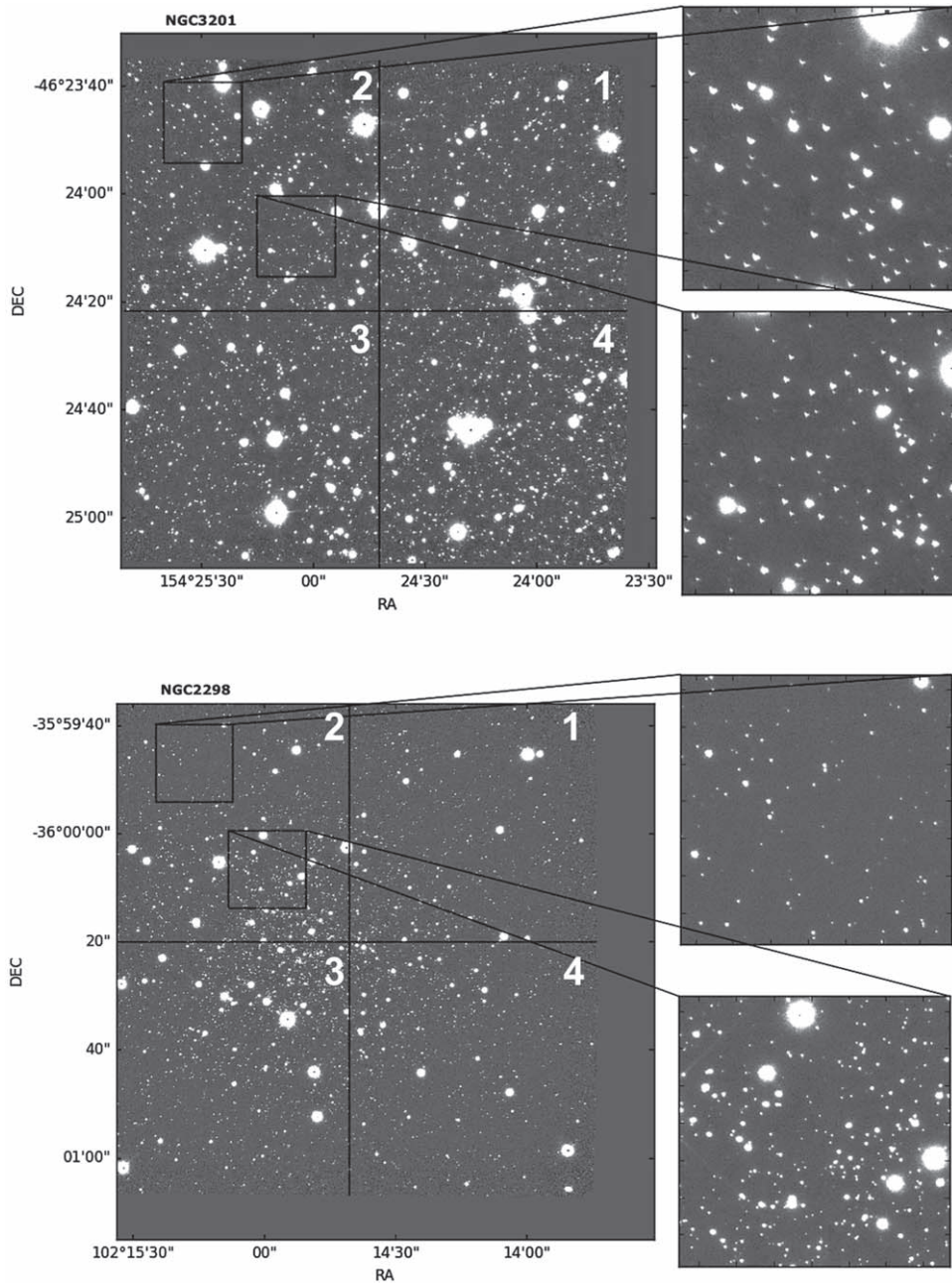


Figure 3. GeMS/GSAOI K_s -band co-added mosaic images of NGC 3201 (top) and NGC 2298 (bottom). The insets show a region of array 2 with a sampling of the worst (top zoom-in image) and best PSFs (bottom zoom-in image). The labels 1–4 indicate the numbering of each array.

3. Analysis

3.1. Photometry

Final PSF-fitting photometry was performed with DAOPHOT-IV/ALLSTAR (Stetson 1994) using a cubically variable PSF, on the mosaicked, stacked image associated with the J , H , and K_s bands. The StarFinder (Diolaiti et al. 2000) and DAOPHOT-II (Stetson 1987) packages were also tested prior to performing the final analysis, but DAOPHOT-IV proved to be the best option for continued analysis. A cubically variable PSF model, only available with DAOPHOT-IV, was required to map the spatial variations in the PSF from CANOPUS, which were compounded by the LGSWFS misalignment problems (see Section 2.2). Stellar positions were known a priori via the *HST*/ACS catalogs for both clusters (Sarajedini et al. 2007),

which are deeper than our own, allowing for forced photometry to be performed. Approximately 100–120 stars were chosen per chip to model the PSF, totaling around 400 over the whole field in order to build a global PSF. A Moffat function of $\beta = 1.5$ was chosen as the best approximation from which to generate the PSF via a χ^2 test using the output of DAOPHOT-IV. Experiments were also conducted varying the number of PSF stars chosen to build the model PSF, but no improvement was seen in the final CMD or in the photometric error distributions, when more than around 400 stars were chosen over the entire field.

While other papers have performed a chip-by-chip photometric approach, generating chip-specific PSFs (Saracino et al. 2015; Turri et al. 2015, 2017), an exploration into any improvement made by performing photometry in this way

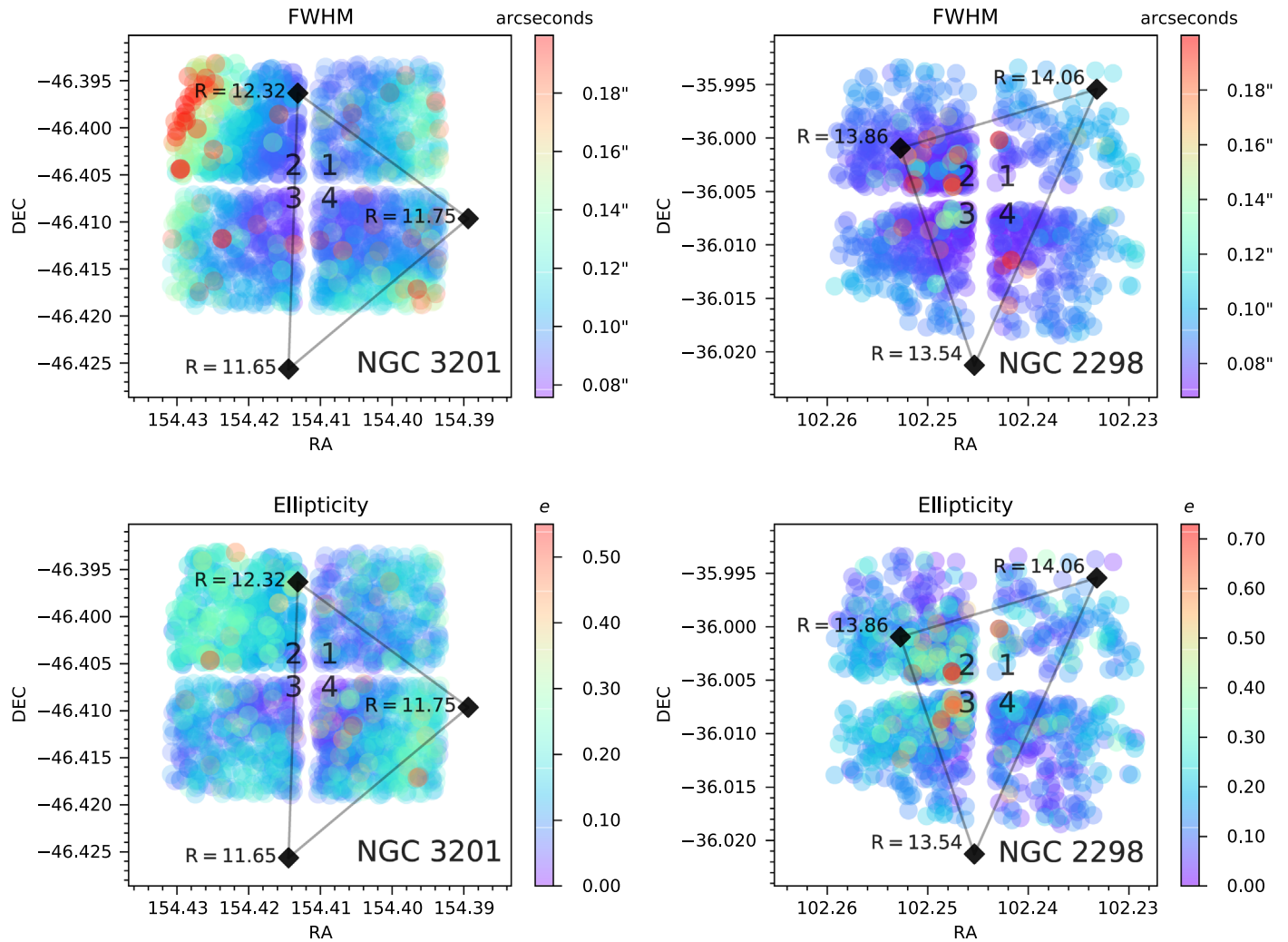


Figure 4. FWHM (top panels) and ellipticity maps (bottom panels) of the NGC 3201 fields (left panels) and NGC 2298 fields (right panels) in the K_s band, created from a sample of ~ 500 stars in the corresponding mosaic, co-added images. The NGS constellation is indicated by the black diamonds and lines, with the R -band magnitudes of the stars labeled correspondingly. The labels 1–4 at the center of the FOV indicate the array numbering.

proved unfruitful. The decision to perform the final photometry on the mosaicked, stacked images was based primarily on the observed temporal variability and quality of the PSF between individual images. In general, irregularities in the PSF in individual images were seen to average out in the stacked image, leading to a more symmetric and uniform PSF in the final stacked image. Additionally, model PSFs were found to be successfully generated more often using the symmetric PSFs found in the stacked images, qualified as smaller fitting residuals in the final PSF-subtracted image. This decision was further supported following an experiment directly comparing magnitudes measured using our own method against those of the chip-by-chip approach. Photometry was performed, chip by chip and exposure by exposure, for the NGC 3201 data taken with the K_s filter, after which an average magnitude was calculated for each data point and compared against the mosaic, stacked measurement using the global PSF. On average the two measurements deviated by only $\sim 1\%$, while the process of chip-by-chip PSF generation often presented substantial difficulties owing to a lack of acceptable stars from which to generate the model PSF. As a precaution, all stars lying in the chip gaps were removed from the final photometric catalog to ensure no instances of repeated measurements due to a star

appearing in more than one chip, a possible result of the dithering pattern. Photometric uncertainties, as provided by ALLSTAR and presented as a function of magnitude, can be seen for NGC 3201 in Figure 5. Note that the photometric catalogs for both clusters were cleaned via 1σ clipping above the mean photometric error for all magnitudes, resulting in the truncated shape of the curves. Figure 5 also shows the improvement to the overall photometric quality of the catalogs following PM cleaning as described in Section 3.3, with the initial 1σ -clipped catalog of NGC 3201 being shown before (left) and after (right) PM cleaning.

3.2. Photometric Calibration

A limitation encountered in deriving the photometric zero-points associated with the GSAOI images was the high resolution provided by the system. Due to the absence of standard-star catalogs derived using a similar resolution, zero-point calibration using standard stars from the 2MASS Point Source Catalog (Skrutskie et al. 2006) was not possible, as most of the bright stars suitable for photometric calibration in the GSAOI images were saturated. Therefore, the photometric zero-point calibration was performed using a two-step process involving intermediate standards. Stars from the 2MASS

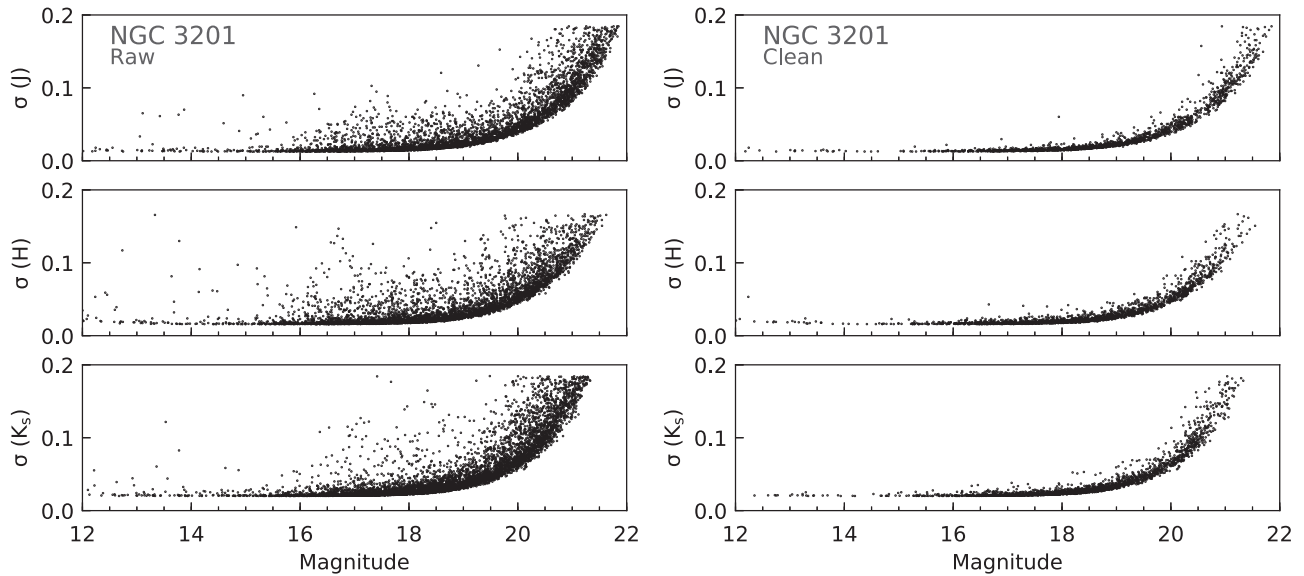


Figure 5. Photometric errors in units of magnitude as a function of magnitude in the JHK_s filters (top to bottom panels), for the cluster NGC 3201 following 1σ clipping, before (left) and after (right) PM cleaning.

catalog were identified and used to calibrate wider-field, but lower-resolution, images that included the GSAOI fields. Then, well-isolated stars in the GSAOI frames were identified in the wide-field images and used as secondary standards to calibrate the GSAOI images to the 2MASS system. In the case of NGC 3201, archival ESO-VLT/HAWK-I JHK_s images were used for the calibration. No archival data were available for NGC 2298, so we obtained JHK_s imaging using FLAMINGOS-2 at Gemini-South during the night of 2016 August 6–7 as part of program GS-2016B-Q-56. Both data sets were processed with THELI, using a method similar to the one described in Section 2.3. Instrumental magnitudes for nonsaturated stars within the calibration data sets were obtained using aperture photometry, performed using different radii with the IRAF¹⁹ task PHOT inside the DAOPHOT package. The measured magnitudes were then corrected by the aperture variation prior to calibration to the 2MASS photometric system. The GSAOI images were then photometrically calibrated using the same approach, and aperture photometry was performed using a set of well-isolated nonsaturated stars found in common with the HAWK-I and FLAMINGOS-2 images, from which the GSAOI frames were calibrated. For all bands, a zeroth-order polynomial (constant) fitting to the difference in magnitude between GSAOI and HAWK-I/FLAMINGOS-2 data was used to derive the final zero-points. Table 3 shows the photometric zero-points determined for the JHK_s filters. Note that unless otherwise stated, all magnitudes presented in this paper are in the Vega magnitude system.

3.3. Proper-motion Cleaning

In order to make our CMDs as uncontaminated as possible, we performed relative PM measurements of all objects in both GCs, using the PM vector distributions to select high-likelihood cluster members. The GSAOI (x, y) position catalogs that were used correspond to the centroid positions

¹⁹ IRAF is distributed by the National Optical Astronomy Observatories (NOAO), which is operated by the Association of Universities for Research in Astronomy (AURA), Inc., under cooperative agreement with the National Science Foundation.

Table 3
2MASS Zero-points

Filter	NGC 3201	NGC 2298
J	26.403 ± 0.017	25.098 ± 0.012
H	26.476 ± 0.02	25.285 ± 0.023
K_s	25.696 ± 0.017	24.443 ± 0.034

Note. Vega mag photometric zero-points, determined using 2MASS stars in HAWK-I images for NGC 3201 and in imaging data from Flamingos-2 for NGC 2298, as described in Section 3.2.

obtained from the DAOPHOT PSF-fitting photometry, performed chip to chip and exposure by exposure, contrary to our final photometric method used for isochrone fitting. As the PM cleaning necessitates more accurate centroiding, photometric precision was sacrificed, again quantified through the fitting residuals. We chose to use the K_s -band images to calculate relative PMs, as this filter provided the best FWHM (see Table 2). The counterpart catalogs from the *HST*/ACS GC Survey provided the ACS camera (x, y) coordinates, which are distortion-free and, hence, can be used as the reference frame and as first-epoch positions.

The precision of PM measurements is largely determined by the ability to remove the different distortion effects in the camera optics. Unfortunately, the different distortions present in MCAO instruments are very hard to model from first principles given their complexity, since they likely depend on the specific observing conditions and instrument configurations (e.g., offsets, relative position of the NGS and LGS constellation, etc.). For the case of GeMS/GSAOI, in addition to anisoplanatism, other distortions caused by gravity flexure or movement of the AO bench have been suggested (Neichel et al. 2014a). In a recent study by Massari et al. (2016), combined GeMS/GSAOI and *HST*/ACS data were used to measure the astrometric capabilities of the GeMS/GSAOI instrument. The authors used previous *HST*/ACS PM measurements in the NGC 6681 field to isolate and directly measure the distortion effects in GeMS, which they report to reach maximum amplitudes between -1.64 and 4.83 pixels in x and between

–0.49 and 0.35 pixels in y . Given these considerations, we chose to remove such distortions using a chip-by-chip and exposure-by-exposure approach. However, we point out that at no point were we interested in or attempting to measure absolute PMs. Our analysis aims at reducing the impact of GSAOI field distortions in order to obtain relative PMs for the decontamination of cluster-member stars, as well as testing the astrometric capabilities obtained from the experimental design of our survey.

To begin with, we cross-matched the stars in both epoch catalogs using the approximate R.A. and decl. coordinates obtained from the GSAOI image header. In the case of NGC 3201, the transformation was calculated using the stars classified as cluster members in Simunovic & Puzia (2016). For NGC 2298 we used the preliminary catalog of the *HST* UV Legacy Survey of GCs (Piotto et al. 2015; Soto et al. 2017) to select stars with displacement values $D_x, D_y = 0$ (see Table 2 in Soto et al. 2017), i.e., stars whose PMs are consistent with the cluster’s motion. This way we effectively removed large intrinsic stellar motions, leaving only the cluster’s mean motion and the distortion effects left to be fit. We then used the GEOMAP task from IRAF to calculate geometric transformations in order to map the GSAOI (x, y) pixel coordinate system onto the reference ACS (x, y) pixel coordinate system. Within the GEOMAP task, we used “general” for the fit geometry. With this option, a linear term and a distortion term are computed separately. The linear term includes an x and y shift, an x and y scale factor, a rotation, and a skew parameter. The distortion term consists of a third-order polynomial fit to the residuals of the linear term, therefore increasing the number of coefficients to nine per axis. We also included the option for a 3σ -clipping iteration on the residual values in order to remove any remaining outliers. The transformation was then applied with the GEOXYTRAN task within IRAF to the entire GSAOI catalog, chip by chip and exposure by exposure. Based on previous works that have studied the geometric distortions of the GeMS/GSAOI field (Neichel et al. 2014a; Dalessandro et al. 2016; Massari et al. 2016), we expected our transformed coordinate system to be distortion corrected down to ~ 1 mas. In particular, Neichel et al. (2014a) found that for single-epoch, nondithered data, astrometric precision of ~ 0.2 mas was possible for bright stars and 60 s exposures. For our case of dithered data with 30 s exposures, they predict around ~ 0.2 – 0.5 mas precision (see their Figure 17), while both Massari et al. (2016) and Dalessandro et al. (2016) report an astrometric accuracy of ~ 1 mas for high stellar density fields. Therefore, we expected to reach a precision in the ~ 0.2 – 1.0 mas range, which we considered to be sufficient for our intended relative PM decontamination.

To explain our method of PM cleaning, let us define (x'_{ij}, y'_{ij}) as the transformed GSAOI star coordinates for chip i and exposure j and $(x_{\text{ref}}, y_{\text{ref}})$ as the reference ACS star coordinates. We combined all exposures for chip i and calculated the average positions, (\bar{x}'_i, \bar{y}'_i) . The error of the average value for a given coordinate ν was then calculated as $\sigma_{\bar{\nu}} = \sqrt{\sigma_s^2/N}$, where $\sigma_s^2 = (N-1)^{-1} \sum_k (\nu'_k - \bar{\nu})^2$ is the unbiased estimate of the sample variance and N is the number of detections. The final catalog was then a combination of all chips, selecting only stars with at least four detections, which provided the coordinates (\bar{x}', \bar{y}') . In Figure 6 we show the obtained astrometric error²⁰ for

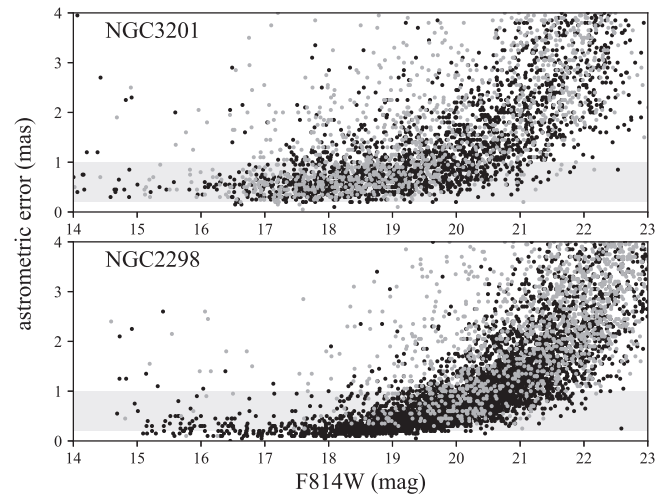


Figure 6. Astrometric error as a function of F814W magnitude for NGC 3201 (top panel) and NGC 2298 (bottom panel). The gray points correspond to the rejected stars in the vector point diagram selection (see Figure 7). The shaded regions mark the 0.2–1.0 mas range for the precision expected based on similar studies in the literature (Neichel et al. 2014a; Dalessandro et al. 2016; Massari et al. 2016). Note the comparatively worse performance in the NGC 3201 data due to the PSF degradation explained in Section 2.2.

stars in NGC 2298 and NGC 3201 as a function of magnitude (gray and black points are explained further below). In both cases we observed an astrometric precision consistent with the expected performance as explained earlier, although the degradation of the PSF in the NGC 3201 data (see Section 2.2) evidently contributed to comparatively worse astrometric precision. However, it is clear that with good AO correction one can achieve submilliarcsecond astrometric precision down to $F814W \simeq 20$ mag within a few minutes on GSAOI.

We then calculated the PMs in ACS pixel units $\delta x = \bar{x}' - x_{\text{ref}}$ and $\delta y = \bar{y}' - y_{\text{ref}}$ and used them to construct vector point diagrams. We did this by separating the entire luminosity range into five magnitude bins and constructing vector point diagrams for each bin. The cluster member selection was then done as follows: first, we calculated the standard deviation of the value $R = \sqrt{\delta x^2 + \delta y^2}$ for each bin, and then we selected as cluster members only those stars that had $R < 1\sigma_R$ for each individual magnitude bin. This conservative threshold helped us reject the stars with a comparatively worse PSF and astrometric precision, such as bright saturated stars and stars near the edge of the detectors.

The results of the PM selection are illustrated in Figure 7 for NGC 3201 and NGC 2298, where the black and gray points show the selected members and nonmembers, respectively, as also shown in Figure 6. The vector point diagrams for each magnitude bin are shown accordingly in the subpanels next to each CMD. The black lines in each subpanel show the density histograms for horizontally and vertically binned data. The red lines show Gaussian probability density function (pdf) fits to the binned data. Indeed, the measured PMs of the central clump in the vector point diagrams are typically well fit with a Gaussian pdf, which supports our cluster member selection using a sample dispersion estimate such as the standard deviation. Note that the distribution becomes broader for fainter (i.e., less massive) stars,²¹ which is expected from both

²⁰ Pixel units were converted to mas units by using the plate scale $0''.05 \text{ pixel}^{-1}$ that corresponds to the ACS/WFC camera.

²¹ The brightest bin can be ignored since it has a relatively low number of stars, in addition to the star’s measured centroids being more affected by saturation.

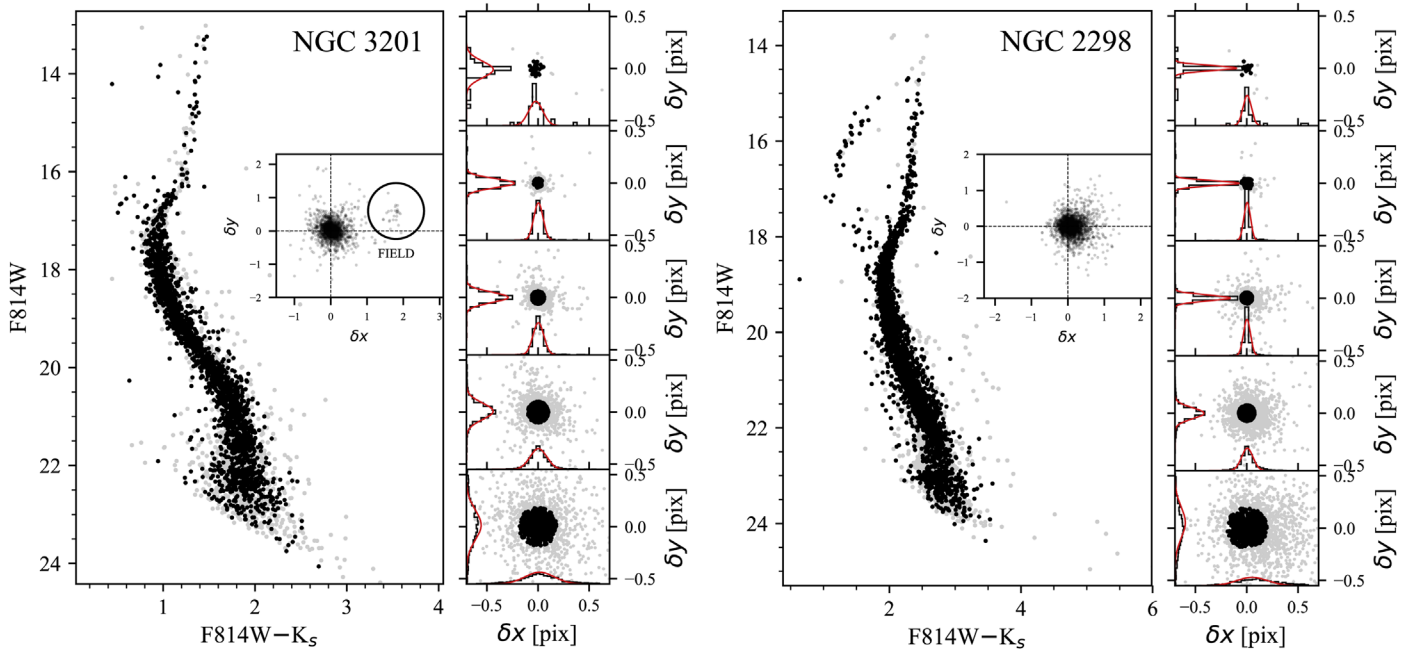


Figure 7. *HST*-Gemini CMDs of cluster members (black points) and nonmembers (gray points; also shown in Figure 6) for NGC 3201 (left) and NGC 2298 (right), as measured in the combined optical–near-IR filters. The vector point diagrams are shown for five magnitude bins in each cluster, with the corresponding color-coding for selected cluster member and nonmember stars. The black lines in each subpanel show the density histograms for horizontally and vertically binned data. The red lines show Gaussian pdf fits to the binned data. Additional inset panels in the CMD plots show the vector point diagrams of the whole catalog for each cluster.

photometric errors and energy equipartition. This justifies the use of separate vector point diagrams at different magnitude bins for the cluster member selection. Also, we note that the CMDs are almost unaffected by the PM cleaning, which is explained by the seemingly low contamination of field stars inside the fields covered by the GSAOI data. Only for NGC 3201 are we able to clearly distinguish a small number (~ 30) of field stars²² in the data, as shown in the inset panels. Moreover, the rejected stars (gray points) in Figure 7 are shown in Figure 6 to discriminate what our rejection is based on. In the case of NGC 2298, the relatively superior astrometry means that we were able to recover the full intrinsic stellar motion distribution for the brighter bins and reject mostly the few objects with a poorer astrometric precision. In contrast, for the fainter magnitudes the PM threshold becomes more strict than the full stellar motion distribution, and hence we started rejecting at the tails of the velocity distribution. In the case of NGC 3201, the relatively poorer astrometry and closer heliocentric distance (see Table 1) result in our PM threshold always being comparable (or smaller) to the full intrinsic stellar motion distribution, and hence the selected members and nonmembers share the same distribution in Figure 6, as one would expect for a nonbiased selection. In conclusion, a large fraction of the rejected stars likely corresponded to actual cluster members on the tails of the velocity distribution; hence, these particular cluster-member samples are not representative of the full internal dynamical distribution, but are rather more robust noncontaminated samples. The main goal of including the PM measurements in this paper is for the opportunity to test the astrometric capabilities obtained from the experimental design of our survey, as demonstrated in the next paragraph.

²² This is due to the lower galactic latitude of NGC 3201, i.e., $b = 8^\circ 64'$, compared to $b = -16^\circ$ for NGC 2298.

In a recent work, Simunovic & Puzia (2016) measured PMs using multiepoch *HST* imaging data for the central regions of a large sample of GCs. Their sample included NGC 3201, which allowed us to compare the PM measurements for all stars in common in both studies. We transformed all PMs from the ACS/WFC pixel units into the more common mas yr^{-1} units by assuming the ACS/WFC pixel scale equal to $0''.05 \text{ pixel}^{-1}$ and divided by the time baseline ($\sim 7 \text{ yr}$) between the first and second epoch. We then compared the PMs measured for each sky coordinate in Figure 8. The top two panels show only a sample of stars with relatively well constrained PMs. Specifically, we include only the stars with PM errors $\sigma \leq 0.1 \text{ mas yr}^{-1}$, as calculated using the formula previously shown. Adding in quadrature the maximum error contribution from both measurements gives $\sqrt{(0.1)^2 + (0.1)^2} = 0.14 \text{ mas yr}^{-1}$, which agrees nicely with the measured scatter around the linear relation, shown in the panels as the rms deviation values. The scatter increases by a factor of two for the bottom panels, which includes all stars in common. A more detailed analysis on this comparison is beyond the scope of this work, but this simple test shows that the measured PMs in this work can reach a similar accuracy to the ones in Simunovic & Puzia (2016), which are entirely based on *HST* data. This suggests a promising potential of the astrometric capabilities of the GeMS/GSAOI instrument when combined with *HST*-based data, as found also by recent similar studies (Dalessandro et al. 2016; Massari et al. 2016).

The PM-cleaned catalogs of NGC 3201 and NGC 2298 are used throughout the rest of this work for the characterization of the CMDs and comparison with stellar evolutionary models.

3.4. Differential Reddening

Prior to isochrone fitting and determination of the best-fit isochrone, we determined the DR corrections for all optical (F606W and F814W) and UV (F336W and F438W) bands. No DR correction was applied to the near-IR filters, as this was

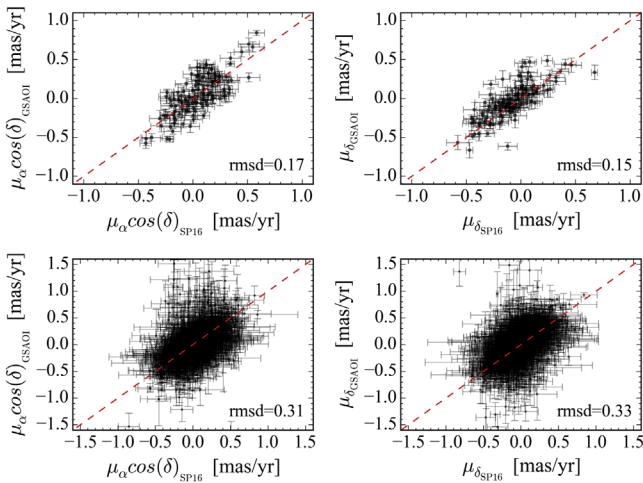


Figure 8. PMs measured in sky coordinate units in NGC 3201 vs. the ones measured by Simunovic & Puzia (2016) for a sample of stars in common. The top two panels show only stars with PM errors $\sigma \leq 0.1 \text{ mas yr}^{-1}$. The observed scatter around the linear relations is shown in the panels as the rms deviation values. The scatter increases by a factor of two for the bottom panels, which include all stars in common. The panels show good agreement between both studies, and the scatter observed is consistent with the estimated errors.

found to be smaller than or comparable to the photometric uncertainties for those filter magnitudes. The choice to determine DR corrections was made in an effort to minimize the contribution of external errors to any detected spread in color space. By accounting and correcting for a spread in color space due to any DR, the accuracy and fidelity of subsequent isochrone fitting were improved. Due to the need for an abundant number of stars and a well-defined fiducial line in the CMD, we calculated the effects of DR using the Soto et al. (2017) *HST* catalogs for both clusters, utilizing the larger *HST* FOV. To determine the DR corrections applied to our catalogs, we followed a method inspired by previous literature.

We chose to adopt the methodology presented in Milone et al. (2012a). This method consists of measuring the local DR affecting one single cluster star, by measuring the median shift along the reddening vector in a sample of nearby MS stars and then repeating this measurement for every single star in the cluster catalog. The median shift is measured with respect to the MS fiducial line, using the 20 nearest MS stars to the target star for which we calculated the local DR correction. As described in Milone et al. (2012a), the median shift along the reddening vector is best seen when the CMD axes were rotated to align the horizontal axis with the reddening vector. The axes were rotated counterclockwise around the point that corresponded to the MSTO, by an angle defined as

$$\theta = \arctan\left(\frac{A_{F814W}}{A_{F606W} - A_{F814W}}\right), \quad (1)$$

where the extinction coefficients A_{F606W} and A_{F814W} are obtained by interpolating the extinction values for *HST*/*ACS* filters from Table 3 in Bedin et al. (2005). The interpolated extinction values are calculated for the corresponding E_{B-V} of NGC 3201 and NGC 2298 found in the McMaster (Harris) Catalog (Harris 1996, 2010 Edition). Once the CMD axes are rotated, a measurement of the shift in values with respect to the fiducial line is taken directly from the x -axis. The median shift

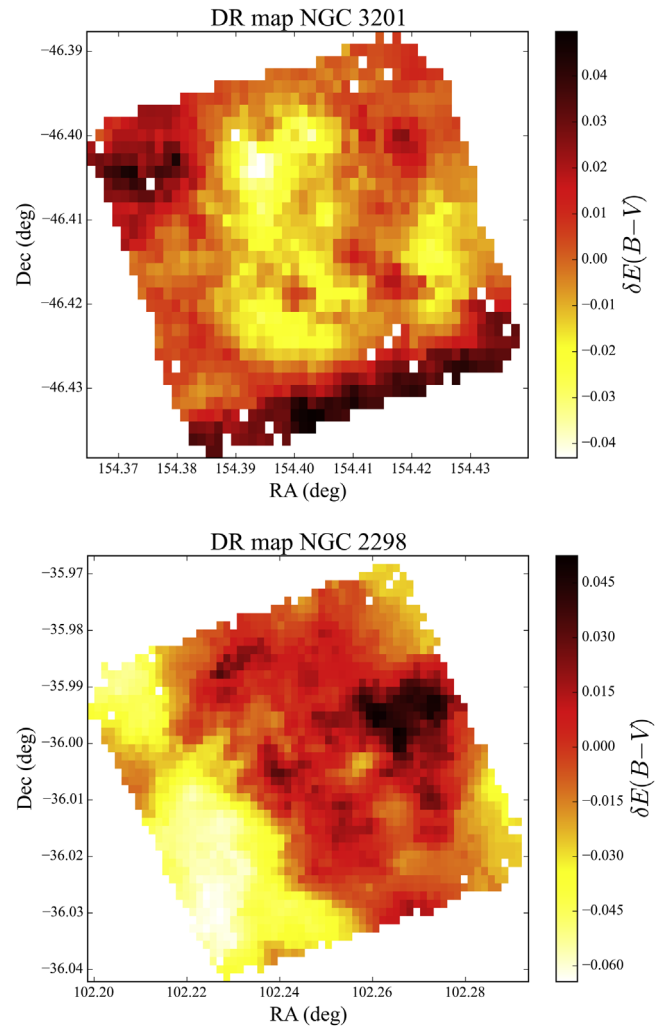


Figure 9. DR maps for NGC 3201 (top) and NGC 2298 (bottom). Both star catalogs were divided into bins of $0'.09$ in both sky coordinate axes. The color map represents the average value of δE_{B-V} for a given binned region of the field.

value is then calculated for the sample of nearby MS stars and taken as the local DR, which is then subtracted from the target star. An illustration of the previous steps is shown in Figure 6 of Milone et al. (2012a).

By applying this process to all the stars, we generated a more defined MS before calculating the fiducial line in the rotated CMD again. The procedure was iterated through two more additional times, after which we assumed a fully DR-corrected CMD. The coordinates were then transformed back to the original F814W versus F606W–F814W plane. By comparing the corrected magnitudes to the noncorrected magnitudes, we used the extinction law cited above to calculate the DR δE_{B-V} for each star and to construct a DR map for our two cluster fields. The DR maps are shown in Figure 9. Using the δE_{B-V} values and the extinction law from Table 3 in Bedin et al. (2005) and Casagrande & VandenBerg (2014, for J , H and K_s), we calculated the DR-corrected magnitudes for each star, for the remaining filters: F336W and F438W. As a summary of the described process, we show the CMDs of NGC 3201 and NGC 2298 before and after DR correction in Figure 10, illustrating the ability of the method to effectively accentuate the features of the CMD.

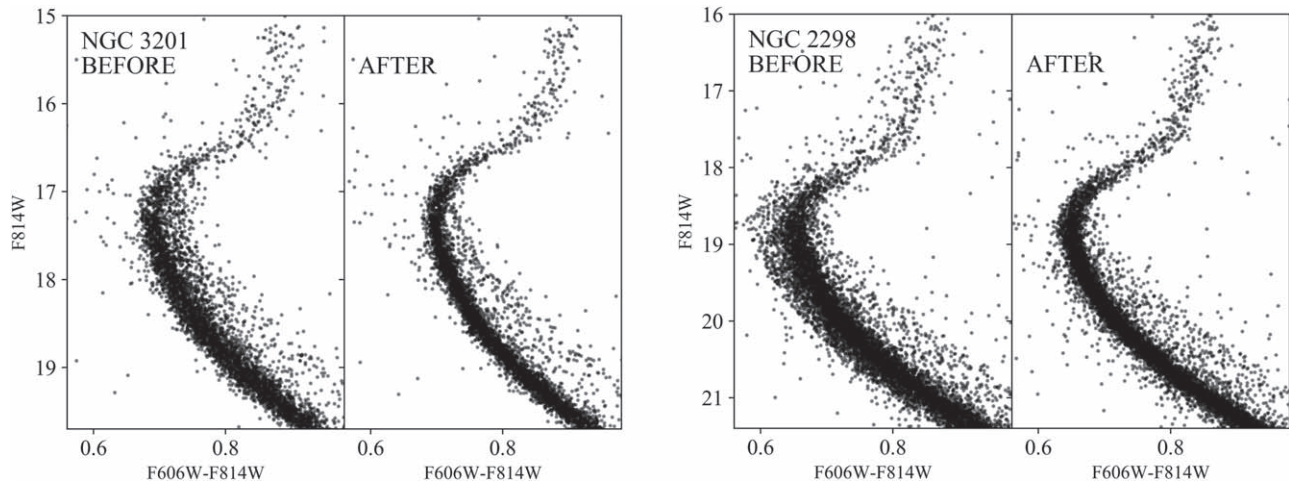


Figure 10. Left: two panels showing the CMD of NGC 3201 before and after the DR correction. Right: same as the left panels, but for NGC 2298. The CMDs are zoomed in to show the region around the SGB and upper MS, where the features are more notably enhanced after the DR correction.

3.5. Photometric Catalogs

Following the calibration of the near-IR photometry PM cleaning and DR correction, master catalogs were created combining the three GSAOI near-IR bands JHK_s together with the two *HST*/ACS optical filters F606W(V) and F814W(I) from Sarajedini et al. (2007), as well as the intermediate data release photometry in the near-UV filter F275W and the two optical filters F336W(U) and F438W(B) from the *HST*/WFC3 *UV Legacy Survey* (Piotto et al. 2015). Mean reddening corrections were not applied directly to the catalogs. Instead, the mean reddening values were determined during the isochrone-fitting procedure described below. During this process, we assumed extinction ratios R_i given by Casagrande & Vandenberg (2014), which yielded reddening-corrected stellar magnitudes via $m_{i,0} = m_i - R_i E_{B-V}$, where m_i is the measured magnitude and E_{B-V} the corresponding reddening. Table 4 summarizes the R_i values for each filter. Caveats associated with this choice will be discussed in subsequent sections.

4. Results

In the following section we utilized the master photometry catalogs to perform absolute age determinations and derive distances, reddening values, and chemical characteristics for the two target clusters. Combining the GSAOI and *HST* photometry proved to be the most diagnostic combination for determining the cluster ages. This is attributed mainly to the clear appearance of the MSK in the faintest measured magnitude regime. As mentioned previously, the combination of the MSK and MSTO is independent of cluster distance and reddening and can, therefore, be used for absolute age determination. We note that earlier studies based on AO-supported imagers, such as VLT/MAD (Marchetti et al. 2007), LBT/PICES (Esposito et al. 2010), and Gemini/GSAOI, have used similar purely ground-based near-IR photometry (Saracino et al. 2016) or combinations of ground- and space-based photometry to study MW GCs (e.g., Moretti et al. 2009; Bono et al. 2010; Monelli et al. 2015; Saracino et al. 2015; Turri et al. 2015; Massari et al. 2016). However, these studies either were not deep enough to sample the MSTO and MSK simultaneously with high-enough photometric quality or did not perform PM cleaning. Our study combines all of these advantages, for the first time.

Table 4

Extinction Ratios from Casagrande & Vandenberg (2014)

	F336W	F438W	F606W	F814W	J	H	K_s
R_i	5.148	4.135	2.876	1.884	0.899	0.567	0.366

Note. The reddening corrections are defined as $m_{i,0} = m_i - R_i E_{B-V}$, where E_{B-V} is determined in the following sections and the extinction ratios R_i for each filter i are the tabulated values.

4.1. Isochrone Models and Stellar Population Parameters

We explore the model dependencies in the age determinations by using the following isochrone sets:

1. Dartmouth Stellar Evolution Database (DSED; Dotter et al. 2008) with $[\text{Fe}/\text{H}] = (-1.59, -1.92)$ dex, $Y = 0.245$, and $[\alpha/\text{Fe}] = 0.2$ dex.
2. Victoria-Regina Isochrone Database (VR; Vandenberg et al. 2014) with $[\text{Fe}/\text{H}] = (-1.59, -1.92)$ dex, $Y = 0.25$, and $[\alpha/\text{Fe}] = 0.2$ dex.
3. A Bag of Stellar Tracks and Isochrones (BaSTI; Pietrinferni et al. 2004) with $[\text{Fe}/\text{H}] = (-1.60, -1.90)$ dex, $Y = 0.246$, and $[\alpha/\text{Fe}] = 0.2$ dex (generated specifically for this work).

We initially used all three isochrone sets to find the CMD regions that showed the maximum dynamic range (i.e., spread in magnitude and color relative to their corresponding uncertainties) prior to determining the age of the GCs. From this study we found that the best filter combination to perform absolute age determination was the K_s versus $F606W - K_s$ combination, a result of the photometric quality of the data in these bands and the ability to narrowly detect the MSK. We also chose to use the F336W versus $F336W - K_s$ combination owing to its added diagnostic power, particularly in the subgiant branch (SGB) region. In the following section, we use these filter combinations to determine the absolute ages of both target GCs, through an exploration of the stellar population parameter space and subsequent pseudo- χ^2 minimization.

We chose to fix the cluster metallicities and $[\alpha/\text{Fe}]$ enrichments using the McMaster Catalog (Harris 1996, 2010 Edition) and Dotter et al. (2010), respectively, following preliminary isochrone fitting to visually assess the fit to the data

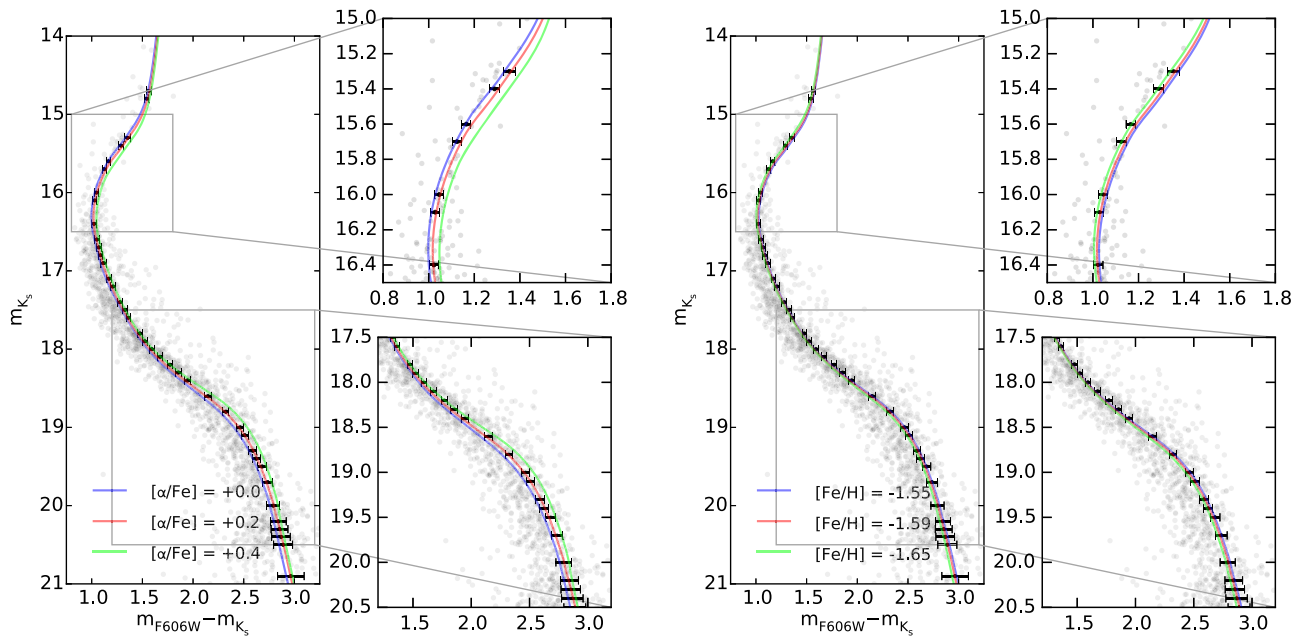


Figure 11. Illustration of the fit dependencies on α -element enrichment (left panel) and metallicity (right panel) with a focus on the SGB and MSK regions, for the case of NGC 3201. Overlaid isochrones were created using the DSED isochrone sample for a best-fit age of 12.2 Gyr, distance of 5.1 kpc, and $E_{B-V} = 0.25$ mag (see Section 4.1). Values of metallicities and $[\alpha/\text{Fe}]$ are listed in the plots, with error bars representing the photometric error associated with a random data point at the given magnitude near the best-fit isochrone.

around the literature values. From this initial investigation, we found that fits to the MS depended weakly on metallicity, while fits to the MSK were somewhat dependent on $[\alpha/\text{Fe}]$, but the chosen value of $[\alpha/\text{Fe}] = 0.2$ demonstrated a good match to the data. These dependencies are shown for the case of NGC 3201 in Figure 11. We do, however, acknowledge the introduction of possible systematic errors related primarily to the choice of an inaccurate α -element enrichment of the isochrone set. In future papers, a full exploration of both chemical and physical parameters will be done for a larger sample of clusters in an effort to limit the effects of any a priori assumptions.

In the following, we explore only the parameter space of distance, reddening, and age to determine the best values and uncertainties in each parameter. The ranges of possible distances and values of reddening were centered about the values given in Table 1. The parameter space exploration was performed in steps of 0.2 kpc in distance and 0.1 mag steps in reddening. Additionally, initial guesses for the ages of 12_{-2}^{+2} Gyr and 13_{+2}^{-1} Gyr were chosen for NGC 3201 and NGC 2298, respectively, based on recent age determinations (Dotter et al. 2010; Muñoz et al. 2013; Wagner-Kaiser et al. 2016).

4.2. A Note on the Use and Nomenclature of the MSK

Throughout this paper, we reference the appearance and recovery of the MSK in the optical–near-IR color combinations of our two clusters. Although we do observe the MSK in both clusters in the optical–near-IR color combinations, we do acknowledge that for the purpose of isochrone fitting we do not recover enough of the knee to anchor our isochrones using this feature alone. Instead, we make use of the so-called “MS saddle,” the point of minimum curvature on the lower MS, to help us anchor our isochrones in the low-luminosity regime. As discussed in Saracino et al. (2018), the MS saddle point is often

misidentified in the literature as being coincident with the MSK. As Saracino et al. explain, the true MSK can only appear completely in pure near-IR CMDs and is a fixed physical feature, while the MS saddle is a purely geometric feature. The authors also discuss the limitations of current isochrone models to accurately predict the position of the MSK, showing that the DSED, VR, and BaSTI models predict different locations of the MSK in the same color combinations. They attribute this disagreement to differing model boundary conditions, leading to different effective temperatures in the regime of the MSK. However, they also find that the three models predict the same location for the MS saddle, but that each model is sensitive to a different parameter influencing the final age determination.

As an example, the BaSTI isochrones were found to be most sensitive to changes in distance between the MSTO and MS saddle, while the DSED isochrones were found to be most sensitive to changes in metallicity (Saracino et al. 2018). As we were limited to 0.5 dex sampling in the creation of our BaSTI isochrones, but not our DSED isochrones, we consider this to be a positive finding. In the following sections we discuss our methodology for fitting the entire MS as part of our age determination, extending down to what we consider to be the recovered MSK. We do, however, point out that a weighting system is introduced to exploit the better-modeled MS saddle and MSTO. As a means of error minimization, we create a ridgeline using overlapping windows, define the MS saddle using the analytical definition alone, as opposed to a geometric method (see Massari et al. 2016), and take into account the photometric errors associated with each data point during final pseudo- χ^2 isochrone fitting. Finally, we caution that the accuracy of following age determinations is subject to the accuracy of both the MS ridgeline and the models themselves.

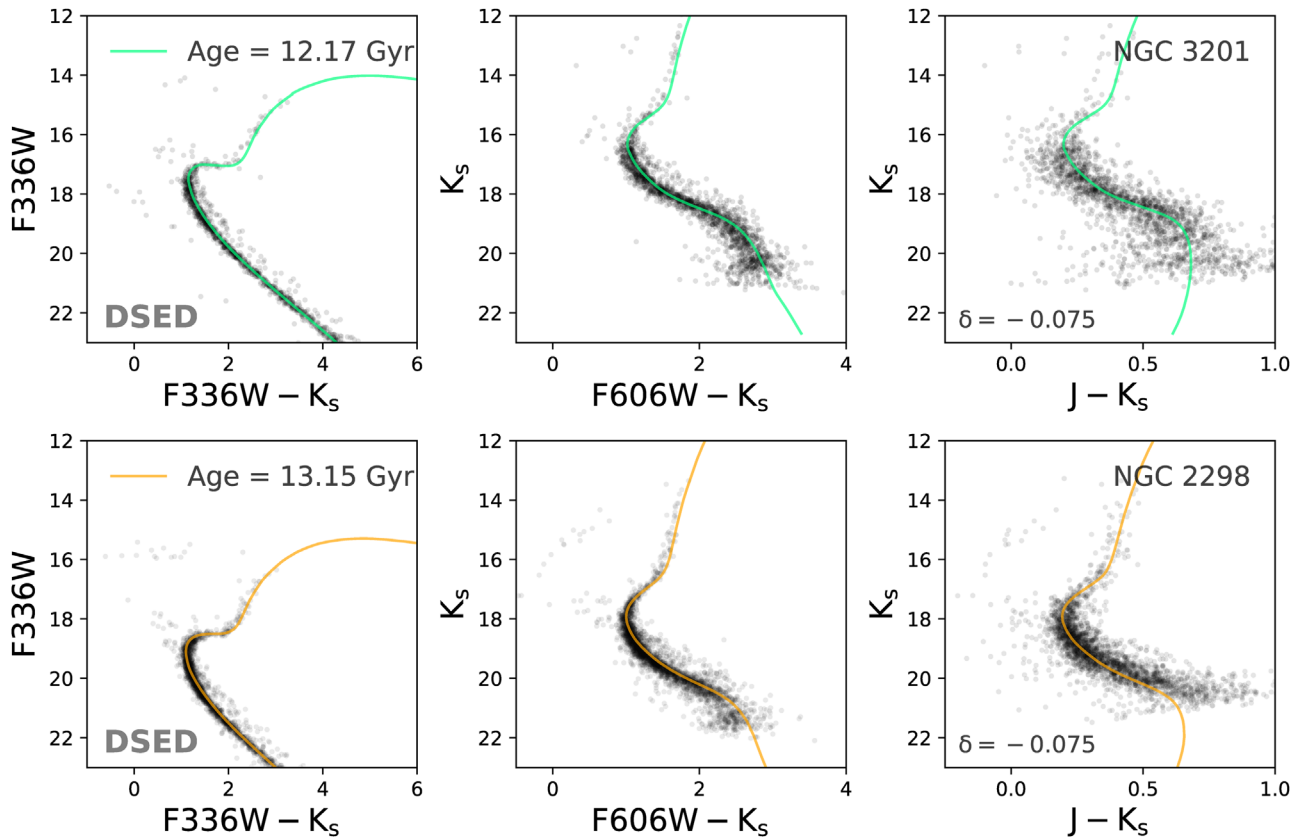


Figure 12. Illustration of the MSK–MSTO–SGB morphologies in various CMDs for NGC 3201 (top panels) and NGC 2298 (bottom panels). We used the best-fit isochrone from the DSED library for both clusters using the derived values of reddening, distance, and stellar population parameters shown in Table 6 based on our PM-cleaned and DR-corrected catalogs (see text for details). We point out that an offset of $\delta(J - K_s) = -0.075$ mag has been applied to the pure near-IR isochrones for both clusters in order to better match the isochrone predictions with the MS.

4.3. Methodology of Isochrone Fitting

To refine the range of possible chemical characteristics and to derive distance and reddening values for the GCs, a study similar to that of Saracino et al. (2016) was performed. We optimized the isochrone fits associated with fixed values of $[\text{Fe}/\text{H}]$ and $[\alpha/\text{Fe}]$ in the aforementioned age ranges by allowing the values of reddening and distance to wander away from the literature values until a true minimum in color–magnitude space was found. In this way we chose to minimize the *distance* in color–magnitude space between each isochrone set and the fiducial isochrone constructed from the data.

4.3.1. Empirical Isochrone Ridgeline Construction

Prior to the color–magnitude distance minimization, an SGB–MS ridgeline, or fiducial isochrone, was constructed, representative of single stars with the most accurate photometry. This was done in order to remove the contamination in color space attributed to stars with larger photometric errors and the binary population. To create the fiducial isochrone, a sliding window was generated in magnitude space, with the window size dependent on the filter combination used for each particular CMD. Seventy stars were found to give robust intra-window statistics, while allowing for efficient rejection of outliers in the K_s versus $F606W - K_s$ color combination, whereas 40 was the corresponding number for the $F336W$ versus $F336W - K_s$ CMD. For each window position, the median magnitude, color, and associated uncertainty given by

the interquartile range of the star sample were recorded as part of the fiducial isochrone creation. After recording said values, the sliding window progressed downward by one star toward fainter magnitudes. This procedure was then repeated sliding along the SGB and MS for different desired color combinations, for both clusters. The resulting ridgelines were then smoothed using kernel sizes of 0.01 mag and examined visually in all desired color combinations to ensure the fidelity of this fiducial isochrone modeling technique, specifically in the presence of significant binary sequences (see Figure 12).

4.3.2. Goodness of Isochrone Fit

We defined a measure of the quality of the isochrone fit by minimizing the offset “ D ” in color–magnitude space between the isochrone and the fiducial ridgeline as

$$D^2 = \frac{1}{N - f} \sum_i^N \frac{(c_{i,\text{fid}} - c_{i,\text{iso}})^2 + (m_{i,\text{fid}} - m_{i,\text{iso}})^2}{\sigma(c_{i,\text{fid}})^2 + \sigma(m_{i,\text{fid}})^2}, \quad (2)$$

where c_i is defined as the color, i.e., $m_{F606W} - m_{K_s}$ and $m_{F336W} - m_{K_s}$, with uncertainty $\sigma(c_{i,\text{fid}})$, and m_i is the magnitude of each star with uncertainty $\sigma(m_{i,\text{fid}})$, summing over all N stars. The parameter f is the number of degrees of freedom, or the number of parameters for which we are solving, which is 3, for mean reddening, distance, and age. This quantity was measured for each point along the isochrone, for both the optical–near-IR and UV–near-IR CMDs, for the case

Table 5
Locations of the Most Diagnostic Regimes (in Apparent Magnitudes) in the Two Chosen Color–Magnitude Combinations and the Chosen Weighting Function Coefficient

Cluster	CMD	m_{MSTO}	$m_{\text{MS-saddle}}$	$\Delta(m_{\text{MSTO}} - m_{\text{MSK}})$	m_{SGB}	a
NGC 3201	$K_s, \text{F606W} - K_s$	[15.8, 16.8]	[18.0, 19.0]	2.20	...	0.15
	$\text{F336W}, \text{F336W} - K_s$	[17.0, 18.0]	0.05
NGC 2298	$K_s, \text{F606W} - K_s$	[17.5, 18.5]	[20.0, 21.0]	2.50	...	0.10
	$\text{F336W}, \text{F336W} - K_s$	[18.0, 19.0]	0.035

Note. Locations of the most diagnostic regimes are defined as the region of minimum curvature (i.e., second derivative crosses zero), in the case of the MS saddle, and the bluest point on the MS, in the case of the MSTO. The location of the SGB is identified empirically as the flattest point in the UV–near-IR CMDs.

of different values of reddening and distance, letting both parameters wander away from the literature values. The minimization of this quantity was then chosen as the desired method for which to determine the absolute ages of the clusters. Additionally, a weighting function, to be described in the following section, was introduced in the calculation of D^2 along the characteristic color–magnitude scale length, $\Delta(\text{MSTO} - \text{MS saddle})$, and in the regime of the SGB in the case of the UV–near-IR color combination. The process of D^2 minimization was then repeated for each cluster six times, i.e., for each isochrone set (DSED, VR, and BaSTI) in two different color combinations K_s versus $\text{F606W} - K_s$ and F336W versus $\text{F336W} - K_s$, in order to generate six independent determinations of the reddening, distance, and age, associated with each cluster.

The filter-set choice of this method was based on the consideration to anchor the isochrone in a regime independent of reddening and distance, i.e., imaging both the MSTO and MSK, in the case of the K_s versus $\text{F606W} - K_s$ CMD, and to explore the formally most diagnostic region associated with age determination, i.e., the SGB, in the case for the F336W versus $\text{F336W} - K_s$ CMD. This is illustrated in Figure 12, where we show the morphologies of these two CMDs in comparison with the pure K_s versus $J - K_s$ CMD, which shows less overall diagnostic power as a result of the lower quality of the combined photometry. We point out, however, that with deeper near-IR photometry the K_s versus $J - K_s$ CMD is equally or even more diagnostic when compared with the other color combinations, especially at luminosities lower than the MSK. Our preliminary tests show that the MS fainter than the MSK is sensitive to the chemical makeup of the stellar population, i.e., its metal abundance and various element abundance ratios, including light and α -elements. This will be addressed in future papers of this series and is particularly important in light of upcoming third-generation telescopes, like *JWST* and ELT, which will be operating in this wavelength range (Watson et al. 2006; Gilmozzi & Spyromilio 2007; Greggio et al. 2012; Gullieuszik et al. 2014; Kalirai 2018; Tamai et al. 2018).

To better leverage the diagnostic power of the MSTO–MS saddle color–magnitude characteristic scale length, a weighting function was introduced in the K_s versus $\text{F606W} - K_s$ isochrone-fitting process of the entire MS. This is also done for the case of the F336W versus $\text{F336W} - K_s$ CMD, with the weighting function designed to exploit the diagnostic power of the SGB. In both cases the weighting function was subject only to the constraint that a maximum weight of 1.0 was achieved at the location of the MS saddle, MSTO, or SGB, with the weights scaling as a function of distance in color–magnitude

space from these points of reference. Additionally, a multiplicative constant was introduced prior to the square root term as seen in Table 5 in order to ensure that none of the determined weights had a value less than zero. The weight function, designed purely to satisfy the given constraints, thus had the form

$$w = 1 - a\sqrt{(m_{\text{DR1}} - m_{\text{data}})^2 \times (m_{\text{DR2}} - m_{\text{data}})^2}, \quad (3)$$

where “DR1, 2” refers to the magnitude associated with the chosen diagnostic regime, i.e., MSTO, MS saddle, and SGB. In the case of the F336W versus $\text{F336W} - K_s$ CMD, the MS saddle equivalent is chosen to be a point on the lower MS at $\text{F336W} \approx 22$ mag. The locations of the MSTO, MS saddle, and SGB as they appear in the two chosen color combinations are listed in Table 5, along with the aforementioned weighting coefficients. Caveats associated with this choice of method, including the handling of photometric errors and model limitations, will be discussed in subsequent sections.

For each set of isochrones and filter combination, values of D^2 were calculated for each position in the mean reddening, distance, and age parameter space. The choice to rederive values of both reddening and distance was made in order to limit a priori biasing of the age determination process through, for example, the introduction of an adjustment in color space in order to improve the overall isochrone fit, as has been done in previous studies. A value of reddening was determined by first finding the mean D^2 for each E_{B-V} over all distances and ages, $\langle D^2 \rangle$. A second-order polynomial was then fit to $\langle D^2 \rangle$ versus E_{B-V} , with the minimum being the best-fit mean reddening. The uncertainty is then ΔE_{B-V} from the point where $\langle D^2 \rangle$ is $\langle D^2 \rangle_{\text{min}} + 1$ (Figure 13(a)). The distance and age were then determined for the best-fit mean E_{B-V} by projecting the D^2 surface (Figure 13(c)). The D^2 values were summed over all ages, and the best-fit distance was the minimum of a second-order polynomial fit to ΣD^2 versus distance. Likewise, the best-fit age was derived from the projection of D^2 over all distances. As with the reddening, the uncertainties in distance and age were determined where $\Sigma D^2 = \Sigma D^2_{\text{min}} + 1$. Figure 13 gives an example of the process.

The results of the D^2 minimization to determine reddening, distance, and absolute age for our two GCs are summarized in Table 6, illustrated in Figures 14 and 15, and discussed in the following sections.

4.4. NGC 3201

4.4.1. Distance and Reddening Comparison

Examining the results presented in Table 6, we find good agreement regarding the derivations of distance and reddening

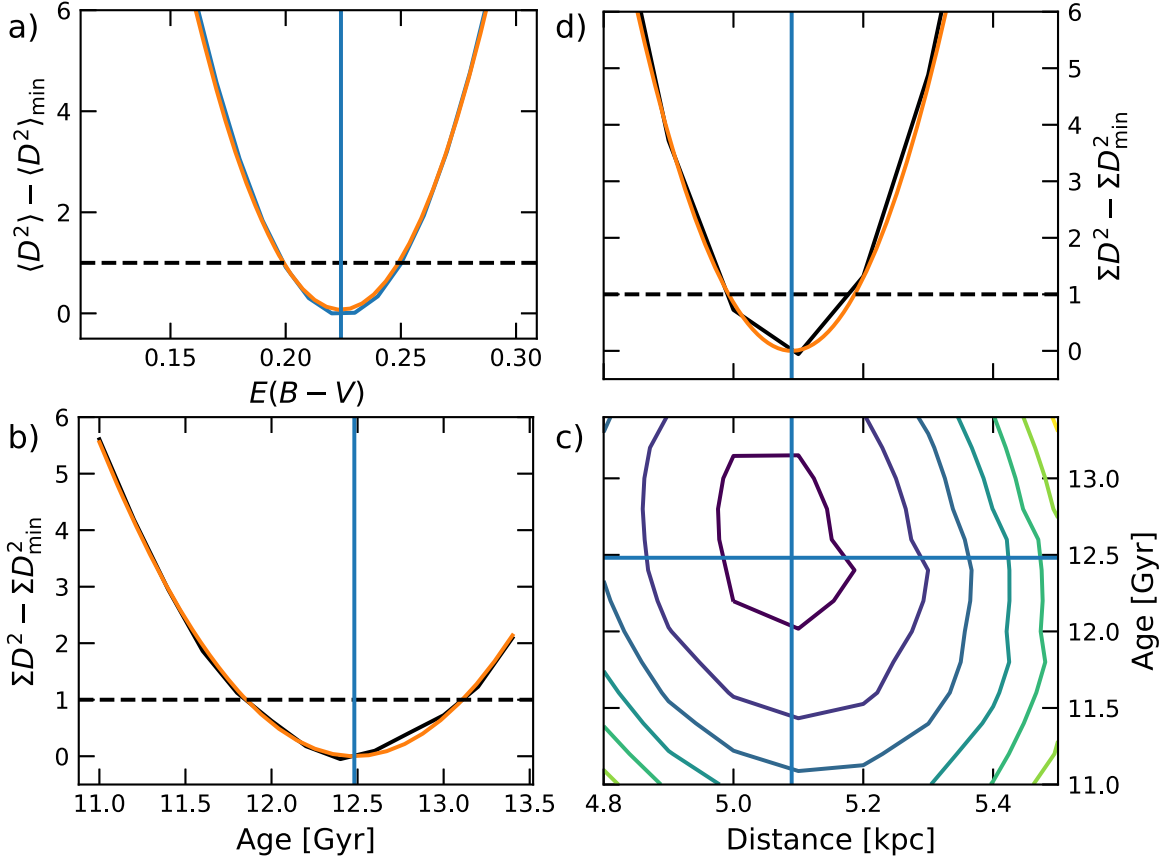


Figure 13. Example of the process for determining the mean reddening values, distances, and ages, with uncertainties, from Equation (2) using DSED model comparisons to the NGC 3201 K_s vs. F606W $- K_s$ photometry. (a) Mean D^2 over all distances and ages as a function of mean E_{B-V} . The minimum of a second-order polynomial fit gives the most likely value of E_{B-V} . The 1σ uncertainty is taken at $\langle D^2 \rangle_{\min} + 1$ (horizontal dashed line). (b) Projection of D^2 over all distances as a function of age; the polynomial fit gives the best age and uncertainty. (c) Contours of D^2 over the distance and age parameter space, with lines indicating the best-fit values of each parameter. (d) Projection of D^2 over all ages to determine the distance.

Table 6
Results of the D^2 Minimization Procedure Described in Section 4.3

Cluster	Model	CMD	Distance (kpc)	E_{B-V} (mag)	Age (Gyr)
NGC 3201	DSED	K_s , F606W $- K_s$	5.1 ± 0.1	0.24 ± 0.02	12.0 ± 0.7
		F336W, F336W $- K_s$	5.0 ± 0.2	0.26 ± 0.02	12.4 ± 0.8
	VR	K_s , F606W $- K_s$	5.0 ± 0.1	0.22 ± 0.03	11.2 ± 0.9
		F336W, F336W $- K_s$	5.0 ± 0.2	0.26 ± 0.03	10.7 ± 1.3
	BaSTI	K_s , F606W $- K_s$	5.1 ± 0.1	0.21 ± 0.02	12.4 ± 0.6
		F336W, F336W $- K_s$	4.9 ± 0.1	0.26 ± 0.02	11.2 ± 2.0
NGC 2298	DSED	K_s , F606W $- K_s$	10.7 ± 0.3	0.17 ± 0.02	13.1 ± 0.6
		F336W, F336W $- K_s$	10.6 ± 0.2	0.22 ± 0.02	13.2 ± 0.6
	VR	K_s , F606W $- K_s$	10.8 ± 0.3	0.13 ± 0.03	14.0 ± 0.9
		F336W, F336W $- K_s$	10.4 ± 0.4	0.21 ± 0.02	12.8 ± 1.3
	BaSTI	K_s , F606W $- K_s$	10.4 ± 0.1	0.14 ± 0.01	13.3 ± 0.5
		F336W, F336W $- K_s$	10.2 ± 0.2	0.22 ± 0.02	12.8 ± 0.9

Note. Errors attached to the determined values are derived as described in Section 4.3.2. In the case of the BaSTI isochrones, conversions from the Bessell & Brett (1988) K band to the 2MASS Skrutskie et al. (2006) system were made using the transformation equation provided by Carpenter (2001): $K_{s,2MASS} = K_{BB} + (-0.039 \pm 0.007) + (0.001 \pm 0.005) \cdot (J - K)_{BB}$.

both internally, within each isochrone set across the two color combinations, and externally, comparing between different isochrone sets. This consistency is illustrated in Figure 16,

using violin plots. We have chosen to select only the most internally self-consistent isochrone set for final age determination, the DSED isochrones. We provide in each panel of

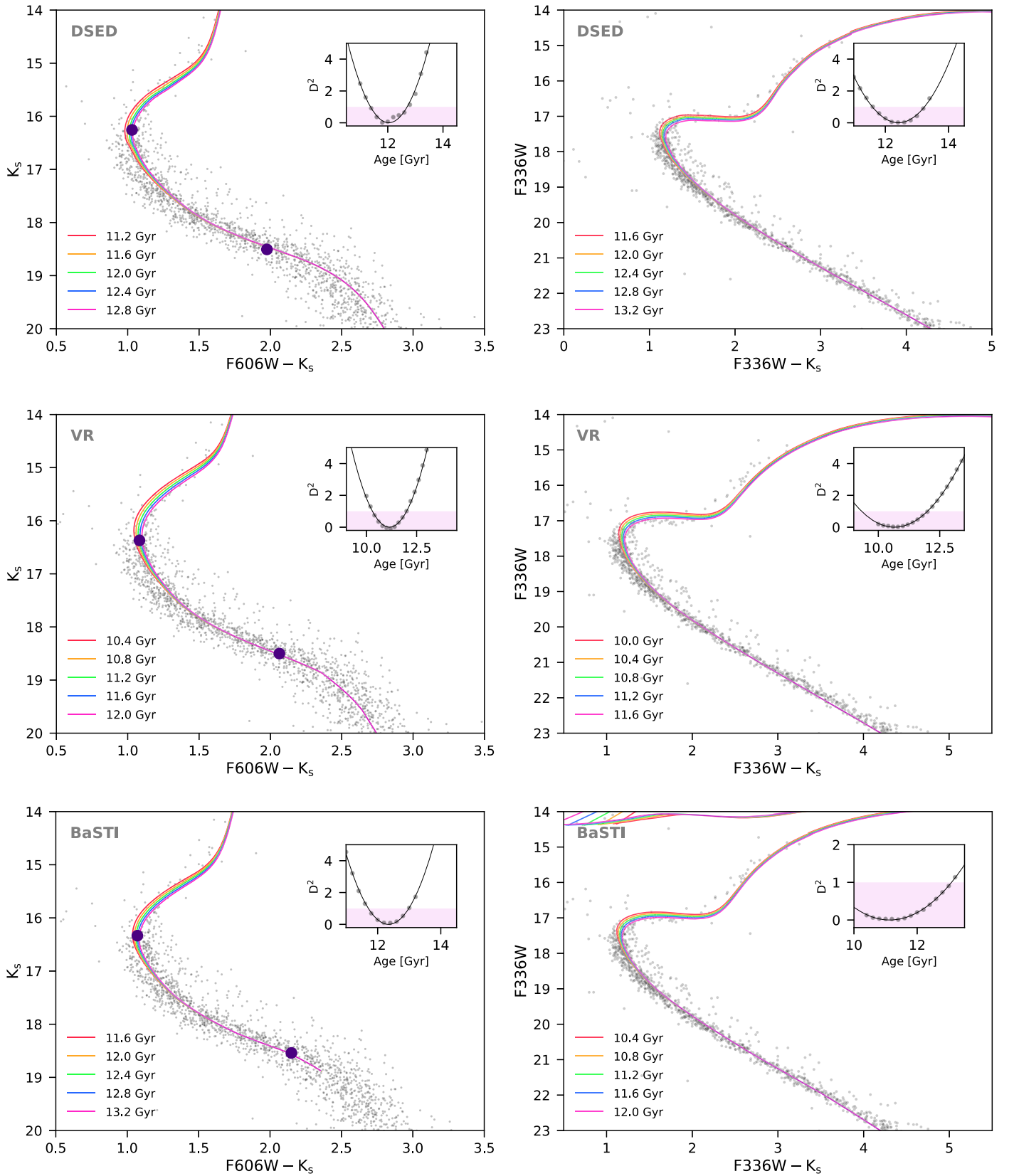


Figure 14. Summary of the D^2 minimization process for NGC 3201 as described in Section 4.3. Top panels: DSED isochrones, with fixed $[\text{Fe}/\text{H}] = -1.59$, $[\alpha/\text{Fe}] = +0.2$, and an age range of 10.0–14.0 Gyr for the optical–near-IR (left panel) and UV–near-IR CMDs (right panels). Middle panels: VR isochrones with $[\text{Fe}/\text{H}] = -1.59$, $[\alpha/\text{Fe}] = +0.2$, and spanning 10.0–14.0 Gyr. Bottom panels: BaSTI isochrones with fixed $[\text{Fe}/\text{H}] = -1.60$, $[\alpha/\text{Fe}] = +0.2$, and spanning 10.0–14.0 Gyr. The insets included in all CMDs show the D^2 values for the various ages, with minimums given in Table 6. The red shaded area spans the lowest D^2 value to a value of 1.0 and defines the range of uncertainty in age.

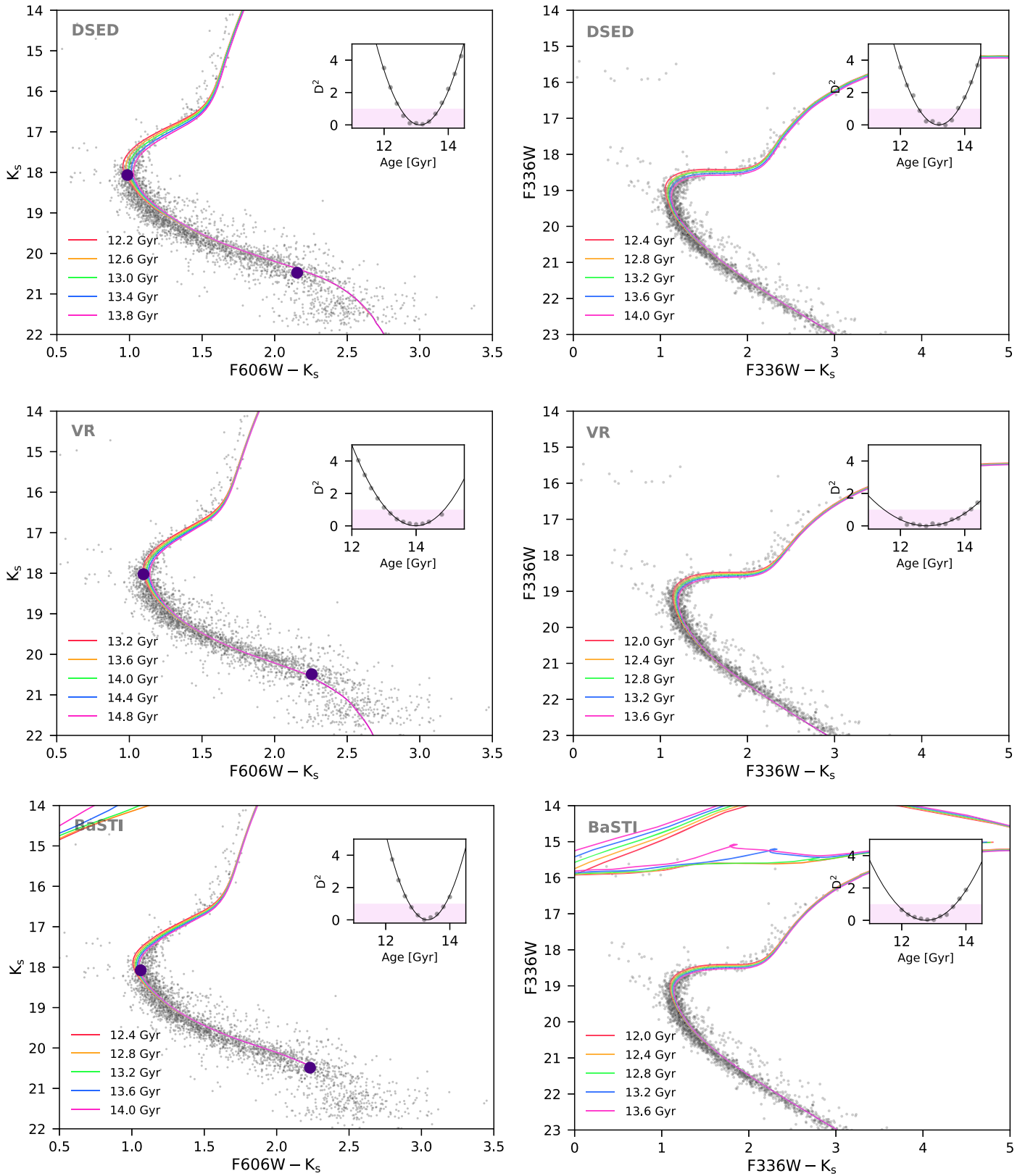


Figure 15. Summary of the D^2 minimization process for NGC 2298 described in Section 4.3. Top panels: DSED isochrones, with fixed $[\text{Fe}/\text{H}] = -1.92$, $[\alpha/\text{Fe}] = +0.2$, and an age range of 12.0–15.0 Gyr for the optical–near-IR (left panel) and UV–near-IR CMDs (right panel). Middle panels: VR isochrones with $[\text{Fe}/\text{H}] = -1.92$, $[\alpha/\text{Fe}] = +0.2$, and spanning 12.0–15.0 Gyr. Bottom panels: set of BaSTI isochrones with fixed $[\text{Fe}/\text{H}] = -1.90$, $[\alpha/\text{Fe}] = +0.2$, and spanning 12.0–15.0 Gyr. The insets included in all CMDs show the D^2 values for the various ages, with minimums given in Table 6. The red shaded area spans the lowest D^2 value to a value of 1.0 and defines the range of uncertainty in age.

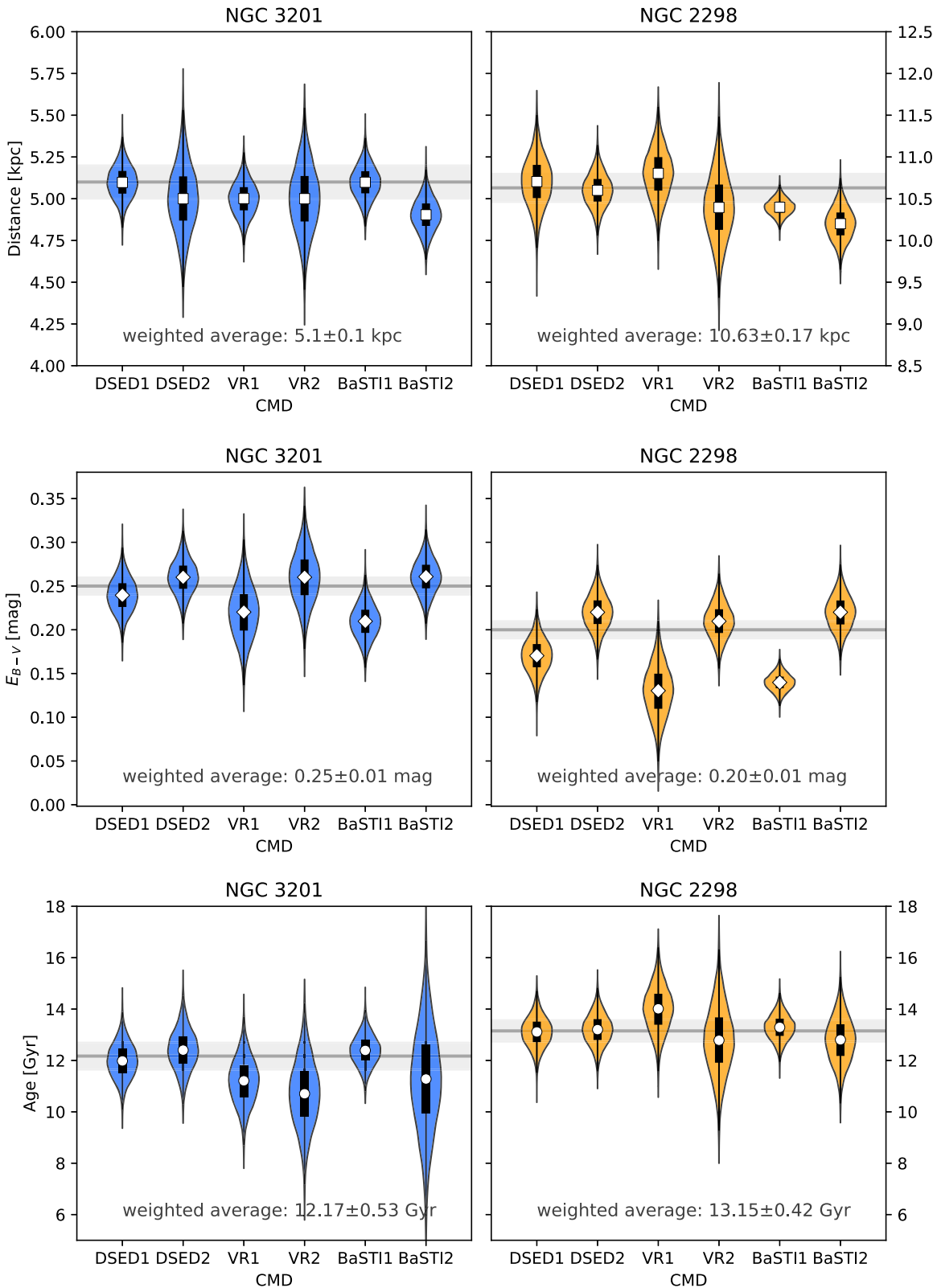


Figure 16. Violin plot comparison of our distance, reddening, and age determinations using the CMD combinations summarized in Table 6 for NGC 3201 (left panels) and NGC 2298 (right panels). The x -axis labels indicate the types of CMDs for each isochrone set, for example, DSED1 corresponds to the K_s vs. $F606W - K_s$ CMD, while DSED2 refers to the $F336W$ vs. $F336W - K_s$ CMD. The same nomenclature is also used for the other two isochrone sets. The horizontal lines and surrounding light shaded regions represent the weighted average and error of the mean using the DSED isochrones, the numerical values of which are given in each panel. Thick black vertical bars inside the violins indicate the $\pm 1\sigma$ uncertainty ranges, while the violins represent the corresponding Gaussian distributions.

Table 7
Comparison of the Derived NGC 3201 Parameters with the Literature

Parameter	Value	Source	Deviation
Distance (kpc)	4.2 ± 0.8	Anguiano et al. (2015)	+0.9
	4.9	Harris (1996, 2010 Edition), Muñoz et al. (2013)	+0.2
$E_{(B-V)}$	4.68 ± 0.24	Bono et al. (2010)	+0.42
	4.6 ± 0.3	Covino & Ortolani (1997)	+0.5
	0.24	Harris (1996, 2010 Edition)	+0.01
	0.24 ± 0.02	Bono et al. (2010)	+0.01
	0.30 ± 0.03	Piersimoni et al. (2002)	-0.05
	0.22 ± 0.03	Covino & Ortolani (1997)	+0.03
Age (Gyr)	0.20 ± 0.02	Alcaino et al. (1989)	+0.05
	$12.836^{+0.277}_{-0.206}$	Wagner-Kaiser et al. (2017)	-0.666
	10.2 ± 0.4	Roediger et al. (2014)	+1.97
	12.0 ± 0.75	Dotter et al. (2010)	+0.17
	11.48 ± 1.27	Bono et al. (2010)	+0.67
	12.0 ± 1.0	Calamida et al. (2009)	+0.17
	13.0–14.0	Layden & Sarajedini (2003)	-0.83
	12.3	Covino & Ortolani (1997)	-0.13

Note. The quoted deviation is in reference to the corresponding values computed using the weighted average of the two CMD types from the DSED isochrones only.

Figure 16 the corresponding weighted average values based on DSED isochrones only.²³ The best-fit isochrone was found to be the $[\text{Fe}/\text{H}] = -1.59$, $[\alpha/\text{Fe}] = +0.2$, $Y = 0.245$ from the DSED isochrone set because, as previously stated, they provide the best internal consistency across distance, reddening, and age measurements and yield the smallest uncertainties. Therefore, we compute the final values of reddening $E_{B-V} = 0.25 \pm 0.01$ and distance 5.1 ± 0.1 kpc using the weighted average of the two DSED isochrones (for the two color combinations). It is these values that are discussed in the following in the context of previously derived literature values.

We obtain results that are in good agreement with previous studies but note a number of discrepancies when comparing our best-fit values against individual works from the literature listed in Table 7 and illustrated in Figure 17. We find the largest literature deviation of ~ 0.9 kpc to be between our NGC 3201 best-fit distance (5.1 ± 0.1 kpc) and the work of Anguiano et al. (2015). However, because of its unusually high uncertainty, the results of Anguiano et al. (2015) are still in agreement to within 2σ of our determination, as is the case of the other literature values with uncertainty margins. We do note, however, that overall our distance determination is slightly larger than all of the literature values. Second, the best-fit reddening value ($E_{B-V} = 0.25 \pm 0.01$) appears significantly lower than the value reported by Piersimoni et al. (2002), but again, it is still within 2σ agreement. All other studies show agreement similar to or better than our result. Third, we observe that our reddening values originating from the UV–near-IR CMDs are systematically larger than those from the optical–near-IR CMDs (see Figure 16).

We stress that in our determination of reddening, particularly referencing the third point discussed above, we have chosen to

fix our extinction coefficient, R_i , and adopt the literature value of E_{B-V} as a starting point in our investigation. Although we decided not to apply a shift in color–magnitude space prior to the age determination in order to achieve a better fit to our isochrones, we felt justified in exploring a range of E_{B-V} values and refer interested readers to Casagrande & Vandenberg (2014), who caution against taking literature reddening values as absolute during isochrone fitting. However, the authors also warn against the use of reddening as a completely free parameter, as it is only one of the many contributing factors to the quality of isochrone fits, and thus this is why we have adopted a literature value as a starting point. In their work, Casagrande & Vandenberg investigated the effects of assuming a constant reddening law and extinction value for all spectral types in a CMD, concluding that it is necessary to either apply a shift in color–magnitude space to an isochrone to best approximate the MSTO or assume different extinction and reddening coefficients depending on the MSTO star type, differing by as much as $\Delta E_{B-V} = 0.05$ and $\Delta R_V = 0.3$. As we have chosen not to apply such a shift, we conclude that our final deviation of up to $|\Delta E_{B-V}| \approx 0.06$ from the literature value is within reason, given the wide SED coverage of our data set. In conclusion, we find that our distance and reddening measurements, subject to the discussed assumptions and uncertainties, range among the more statistically robust parameter determinations and are in good agreement with previously derived values (see Figure 17).

4.4.2. Age Comparison

Subject to the discussed caveats associated with our method and the internal accuracy of the isochrone sets in the regimes deemed most diagnostic for deriving ages, we now present a literature comparison of our final age determination for the cluster NGC 3201, in addition to discussing the strengths and weaknesses of the various isochrone sets. We determine an absolute best-fit age of 12.2 ± 0.5 Gyr, for NGC 3201 using the weighted average from the two CMD types based on only the DSED isochrone set, for reasons discussed in the previous section. Comparing our determined age with those listed in Table 7, we see good agreement, within 2σ for most of the ages listed, including the age determined using the MSTO–MSK method derived by Calamida et al. (2009). However, we find a 4σ – 5σ offset in the case of the age listed in Roediger et al. (2014), though note that the Roediger et al. (2014) value is the youngest of the recent age determinations (see Figure 17). Finally, we note that our age determination is among the best-constrained age determinations listed.

While our final age determination depends primarily on the optimization of the fit to the MSK, MSTO, and SGB, the quality of the fit to other regions of the CMD, in particular to the red giant branch (RGB) in the case of the optical–near-IR color combination, degrades for all the isochrone sets. Figure 14 shows that the isochrone sets consistently predict a redder RGB than is seen in the data. This trend was also observed in earlier studies (Saracino et al. 2016, and references therein) and appears to be due to the isochrone model handling of the near-IR passbands. In the case of the UV–near-IR CMD, the ill-fitted RGB again appears in all three isochrone sets, while the MS is fit best by the DSED isochrone but is sufficiently well fit by all three isochrone sets. However, the BaSTI isochrone fit to the UV color combination only barely demonstrates the discovery of a clear minimum during

²³ We point out that averaging over one isochrone set avoids mixing different prescriptions in the underlying input physics used to generate the various isochrone models. However, the values for the other isochrone sets are provided in Table 6 for transparency, should the reader wish to compute the global average.

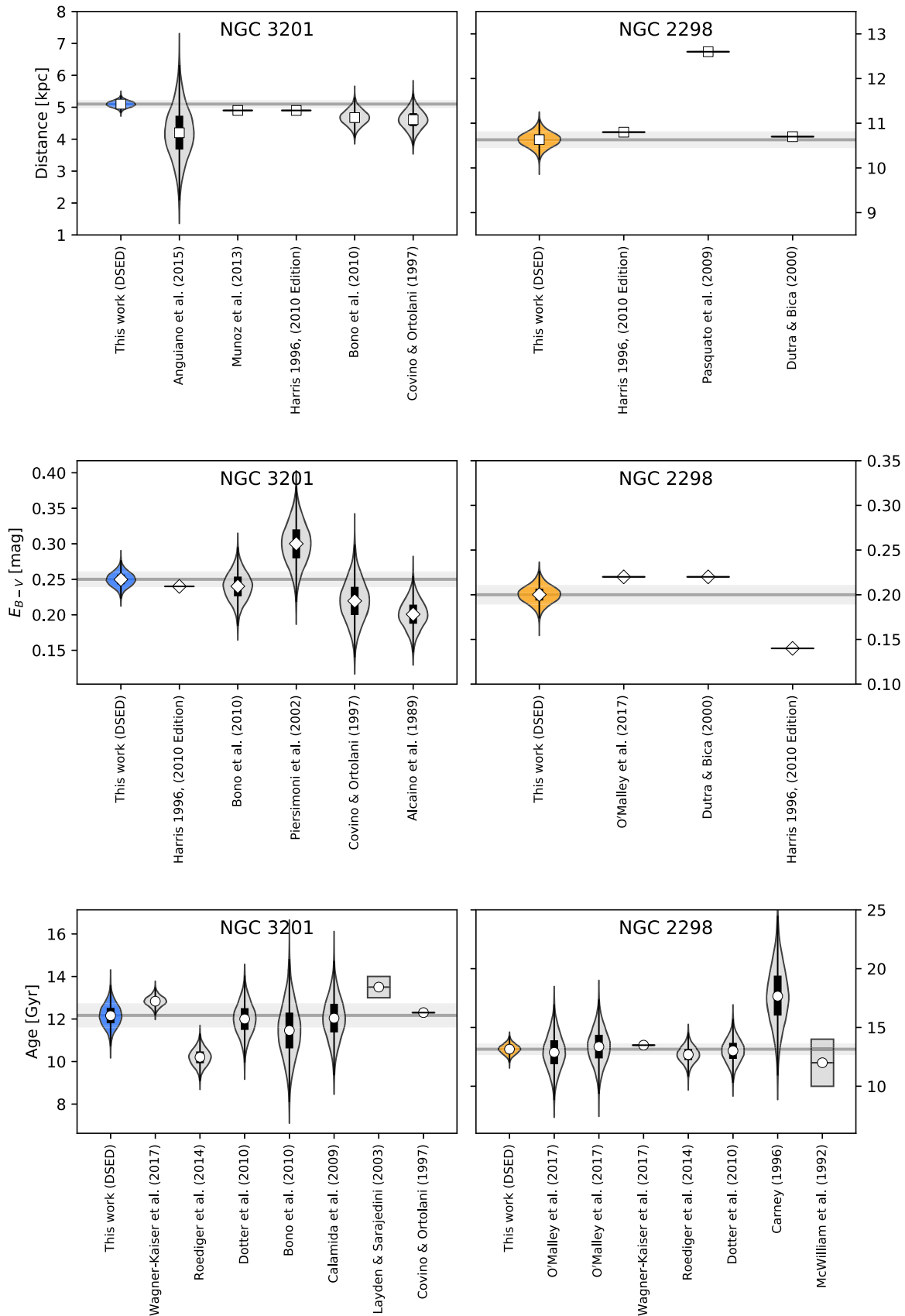


Figure 17. Violin plot comparisons of our distance, reddening, and age determinations with literature values for NGC 3201 (left panels) and NGC 2298 (right panels). The x -axis labels refer to the publications listed in Tables 7 and 8. The horizontal lines and surrounding light shaded regions are as in Figure 16 and represent the weighted mean and error of the mean computed using the DSED isochrones only. The violin labeled “This work” also displays the value. Vertical boxes indicate published ranges, while horizontal bars without vertical spread show literature values for which no uncertainties were given in the corresponding paper. Thick black vertical bars inside the violins indicate the $\pm 1\sigma$ uncertainty ranges, while the violins represent the corresponding Gaussian distributions.

isochrone fitting as can be seen in the inset of the UV CMD in the bottom right panel of Figure 14. This was also the case for the VR isochrone fit to the UV color combination, resulting in large error bars for both the BaSTI and VR age determinations in the UV CMD. Additionally, regarding the fit to the MSTO and MSK, shown as violet circles in Figure 14, all three isochrone sets fit both regions well, with no obvious outliers.

4.5. NGC 2298

4.5.1. Distance and Reddening Comparison

We list the results of isochrone fitting for NGC 2298 in Table 6 and obtain the best-fit distance 10.6 ± 0.2 kpc, again derived using the $[\text{Fe}/\text{H}] = -1.92$, $[\alpha/\text{Fe}] = +0.2$, $Y = 0.245$ DSED isochrone set only, for reasons given in Section 4.4.1. This value is similar to previous determinations (see Figure 17) by Harris (1996, 2010 Edition) and Dutra & Bica (2000) but significantly smaller than the literature distance derived by Pasquato et al. (2009). Even our largest formal distance of 10.8 ± 0.3 kpc, derived for the VR-fit CMD, is starkly inconsistent with the Pasquato et al. (2009) literature value. Additionally, a trend can be observed for the best-fit reddening values, where the optical–near-IR values of E_{B-V} appear systematically lower than from the UV–near-IR CMDs, similar to NGC 3201 (see Figure 16). As discussed above, the reason could be related to changes in the reddening law toward both clusters, which may be different from our assumed law (see Section 3.5). We find a best-fit reddening toward NGC 2298 of $E_{B-V} = 0.20 \pm 0.01$, again adopting the weighted average from the DSED isochrones for comparison with the literature. We find that our value is in very good agreement with previous measurements from O’Malley et al. (2017) and Dutra & Bica (2000) but deviates substantially from Harris (1996, 2010 Edition). We propose that this disagreement could be a result of the methodology used by Harris (1996, 2010 Edition), as integrated-light measurements may suffer from DR issues (see Section 3.4). Although the cause of deviations between the literature and derived values of distance and reddening is not obvious in each case, or easily inferred for this cluster, we note that the deviations in distance are within the expected accuracy of the literature distance measurements (see Bono et al. 2008). Finally, we point out that our distance and reddening determinations mark the only statistically meaningful constraints for NGC 2298 measured thus far (see Figure 17).

4.5.2. Age Comparison

We derive a best-fit age of 13.2 ± 0.4 Gyr for the cluster NGC 2298, using the weighted DSED isochrone set, grouping it among the oldest MW GCs. A comparison of the derived age against literature values is given in Table 8 and illustrated in Figure 17. We find good agreement between our results and previous studies to within $\sim 1\sigma$. Although the literature value from Carney (1996) is ~ 5 Gyr off compared to our value and the rest of the literature, this offset amounts to only $\sim 2\sigma$. Despite the fact that our determined age is among the oldest (modern) ages measured, we find it to be one of the best-constrained CMD age measurements for that cluster found in the literature. The only exception is the value reported by Wagner-Kaiser et al. (2017), who derive an age of $13.493^{+0.007}_{-0.017}$ Gyr from a Bayesian analysis. Given that we use the same ACS photometry as

Table 8
Comparison of the Derived NGC 2298 Parameters with the Literature

Parameter	Value	Source	Deviation
Distance (kpc)	10.8	Harris (1996, 2010 Edition)	−0.20
	12.6	Pasquato et al. (2009)	−2.0
	10.7	Dutra & Bica (2000)	−0.1
$E_{(B-V)}$	0.22	O’Malley et al. (2017), Dutra & Bica (2000)	−0.02
	0.14	Harris (1996, 2010 Edition)	+0.06
Age (Gyr)	12.9 ± 1.5	O’Malley et al. (2017)	+0.25
	13.4 ± 1.5	O’Malley et al. (2017)	−0.25
	$13.493^{+0.007}_{-0.017}$	Wagner-Kaiser et al. (2017)	−0.343
	12.7 ± 0.7	Roediger et al. (2014)	+0.45
	13.0 ± 1.0	Dotter et al. (2010)	+0.15
	17.7 ± 2.5	Carney (1996)	−4.55
	10–14	McWilliam et al. (1992)	+1.15

Note. The quoted deviation is in reference to the corresponding values computed using the weighted average of the two CMD types from the DSED isochrones only.

Wagner-Kaiser et al. (2017), the Bayesian uncertainties may be underestimated.

Examining the isochrone fits presented in Figure 15, we can see that the VR isochrone set reproduces the position of the MSK with the highest fidelity, while all three isochrone sets approximate the MSTO fairly well. Additionally, we observe the same trend as was observed for NGC 3201, namely, that all three isochrone sets predict a redder RGB than what is observed in the data. The VR isochrone best models the data at luminosities below the MSK, with the DSED and BaSTI isochrone sets either lying above the majority of the data points below the MSK or terminating before a trend is established (in the case of the BaSTI isochrone). Considering the fit of the isochrones to the UV–near-IR CMD, all three isochrone sets demonstrate good overall fits from the MS through the RGB. However, all three isochrone sets also appear bluer than the bulk of the data at the MSTO, with the data appearing to “puff up” as the MS transitions to the SGB. This broadening could be the result of uncorrected DR or the result of the presence of multiple stellar populations in this cluster (see Figure 4 in Milone et al. 2012b).

5. Summary and Conclusions

The multi-conjugate AO system, near-IR imager combination, GeMS/GSAOI, mounted on the 8.1 m Gemini-South telescope, was used to observe two MW GCs, NGC 3201 and NGC 2298, reaching a depth of $K_s \simeq 21$ Vega mag for both targets. Spatially variable PSFs were created for both clusters using DAOPHOT-IV in order to perform PSF-fitting photometry, yielding high-quality photometric results. The resulting photometric catalogs were combined with HST near-UV data from Piotto et al. (2015) and HST optical data from Sarajedini et al. (2007) to create panchromatic stellar photometry libraries for both clusters spanning near-UV to near-IR wavelengths. Zero-point calibrations, PM cleaning, and DR corrections were applied to said catalogs to provide clean, precise photometry and to ensure that they contained only high-probability GC member stars. Absolute age determinations were then performed, utilizing a characteristic scale length defined as the distance from MS saddle to MSTO for both clusters. The lower

MSK was recovered in both clusters, for the first time in NGC 2298, highlighting the diagnostic power of AO-supported near-IR data. Three different isochrone sets (DSED, VR, and BaSTI) were used in combination with two CMDs created using UV–near-IR (F336W versus F336W – K_s) and optical–near-IR (K_s versus F606W – K_s) filter combinations to derive values of absolute age, distance, and reddening, adopting values of [Fe/H] and $[\alpha/\text{Fe}]$ derived via high-resolution spectroscopy of member stars. The most internally consistent results were determined using the DSED isochrone-based measurements, yielding age, reddening, and distance determinations for NGC 3201 of 12.2 ± 0.5 Gyr, $E_{B-V} = 0.25 \pm 0.01$ mag, and 5.1 ± 0.1 kpc, respectively. The DSED isochrones were also found to be the most internally consistent set for NGC 2298, yielding age, reddening, and distance determinations of 13.2 ± 0.4 Gyr, $E_{B-V} = 0.20 \pm 0.01$ mag, and 10.6 ± 0.2 kpc, respectively. We find very good agreement between literature values and our derived parameters and show that our measurements are among the most statistically robust constraints determined thus far. New observations for the G4CS are planned in order to apply this method to GCs with a wider range of metallicities and formation histories.

We thank Giampaolo Piotto for kindly providing us with the intermediate data release photometry from the *HST* Treasury Program GO-13297 (Piotto et al. 2015). We thank the anonymous referee for providing constructive remarks that sharpened the results presented in this paper. S.M. would like to thank her collaborators, Gemini Observatory, the Institute of Astrophysics at the Pontificia Universidad Católica de Chile, R. Monty Bird, and the University of Victoria for their support and hospitality and for the incredible learning opportunity provided through the University of Victoria Physics and Astronomy Co-op program. T.H.P. acknowledges support through the FONDECYT Regular Project grant no. 1161817 and from CONICYT project Basal AFB-170002.










This research is based on observations obtained at the Gemini Observatory, which is operated by the Association of Universities for Research in Astronomy, Inc., under a cooperative agreement with the NSF on behalf of the Gemini partnership: the National Science Foundation (United States), the National Research Council (Canada), CONICYT (Chile), the Australian Research Council (Australia), Ministério da Ciência, Tecnologia e Inovação (Brazil) and Ministerio de Ciencia, and Tecnología e Innovación Productiva (Argentina). Additionally, this research has made use of the NASA/IPAC Extragalactic Database (NED), which is operated by the Jet Propulsion Laboratory, California Institute of Technology, under contract with the National Aeronautics and Space Administration.

Facilities: Gemini: South (GeMS/GSAOD); *HST* (ACS, WFC3).

Software: astropy (Astropy Collaboration et al. 2013), matplotlib (Hunter 2007), NumPy (Van Der Walt et al. 2011), IRAF, THELI (Erben et al. 2005; Schirmer 2013), DAOPHOT (Stetson 1987).

ORCID iDs

Stephanie Monty  <https://orcid.org/0000-0002-9225-5822>
 Thomas H. Puzia  <https://orcid.org/0000-0003-0350-7061>
 Bryan W. Miller  <https://orcid.org/0000-0002-5665-376X>
 Eleazar R. Carrasco  <https://orcid.org/0000-0002-7272-9234>

Mirko Simunovic  <https://orcid.org/0000-0002-5652-6525>
 Mischa Schirmer  <https://orcid.org/0000-0003-2568-9994>
 Peter B. Stetson  <https://orcid.org/0000-0001-6074-6830>
 Santi Cassisi  <https://orcid.org/0000-0001-5870-3735>
 Kim A. Venn  <https://orcid.org/0000-0003-4134-2042>
 Aaron Dotter  <https://orcid.org/0000-0002-4442-5700>
 Paul Goudfrooij  <https://orcid.org/0000-0002-5728-1427>
 Peter Pessev  <https://orcid.org/0000-0003-0454-5705>
 Matthew A. Taylor  <https://orcid.org/0000-0003-3009-4928>

References

- Alcaino, G., Liller, W., & Alvarado, F. 1989, *A&A*, **216**, 68
 Anguiano, B., De Silva, G. M., Freeman, K., et al. 2016, *MNRAS*, **457**, 2078
 Anguiano, B., Zucker, D. B., Scholz, R.-D., et al. 2015, *MNRAS*, **451**, 1229
 Astropy Collaboration, Robitaille, T. P., Tollerud, E. J., et al. 2013, *A&A*, **558**, A33
 Balbinot, E., Santiago, B. X., da Costa, L. N., et al. 2011, *MNRAS*, **416**, 1
 Bedin, L. R., Cassisi, S., Castelli, F., et al. 2005, *MNRAS*, **357**, 1038
 Bertin, E. 2006, in ASP Conf. Ser. 351, *Astronomical Data Analysis Software and Systems XV*, ed. C. Gabriel et al. (San Francisco, CA: ASP), 112
 Bertin, E. 2010, SWarp: Resampling and Co-adding FITS Images Together, *Astrophysics Source Code Library*, ascl:1010.068
 Bertin, E., & Arnouts, S. 1996, *A&As*, **117**, 393
 Bessell, M. S., & Brett, J. M. 1988, *PASP*, **100**, 1134
 Bono, G., Stetson, P. B., Sanna, N., et al. 2008, *ApJL*, **686**, L87
 Bono, G., Stetson, P. B., VandenBerg, D. A., et al. 2010, *ApJL*, **708**, L74
 Borysow, A. 2002, *A&A*, **390**, 779
 Borysow, A., Jorgensen, U. G., & Fu, Y. 2001, *JQSRT*, **68**, 235
 Calamida, A., Bono, G., Stetson, P. B., et al. 2009, in Proc IAU Symp. 258, *The Ages of Stars*, ed. Mamajek, Soderblom, & Wyse (Cambridge: Cambridge Univ. Press), 189
 Carney, B. W. 1996, *PASP*, **108**, 900
 Carpenter, J. M. 2001, *AJ*, **121**, 2851
 Carrasco, E. R., Edwards, M. L., McGregor, P. J., et al. 2012, *Proc. SPIE*, **8447**, 84470N
 Carretta, E., Bragaglia, A., Gratton, R., & Lucatello, S. 2009, *A&A*, **505**, 139
 Carretta, E., Bragaglia, A., Gratton, R. G., et al. 2010, *A&A*, **516**, A55
 Casagrande, L., & VandenBerg, D. A. 2014, *MNRAS*, **444**, 392
 Correnti, M., Gennaro, M., Kalirai, J. S., et al. 2016, *ApJ*, **823**, 18
 Covino, S., & Ortolani, S. 1997, *A&A*, **318**, 40
 Dalessandro, E., Saracino, S., Origlia, L., et al. 2016, *ApJ*, **833**, 111
 Diolaiti, E., Bendinelli, O., Bonaccini, D., et al. 2000, *Proc. SPIE*, **4007**, 879
 Dotter, A., Chaboyer, B., Jevremović, D., et al. 2008, *ApJS*, **178**, 89
 Dotter, A., Sarajedini, A., Anderson, J., et al. 2010, *ApJ*, **708**, 698
 Dotter, A., Sarajedini, A., & Anderson, J. 2011, *ApJ*, **738**, 74
 Dutra, C. M., & Bica, E. 2000, *A&A*, **359**, 9
 Erben, T., Schirmer, M., & Dietrich, J. 2005, *AN*, **326**, 432
 Esposito, S., Riccardi, A., Fini, L., et al. 2010, *Proc. SPIE*, **7736**, 773609
 Freeman, K., & Bland-Hawthorn, J. 2002, *ARA&A*, **40**, 487
 Frommhold, L., Abel, M., Wang, F., et al. 2010, *MolPh*, **108**, 2265
 Gilmozzi, R., & Spyromilio, J. 2007, *Msngr*, **127**, 11
 Gratton, R., Sneden, C., & Carretta, E. 2004, *ARA&A*, **42**, 385
 Greggio, L., Falomo, R., Zaggia, S., Fantinel, D., & Uslenghi, M. 2012, *PASP*, **124**, 653
 Gullieuszik, M., Greggio, L., Falomo, R., Schreiber, L., & Uslenghi, M. 2014, *A&A*, **568**, A89
 Gustafsson, M., Frommhold, L., Li, X., & Hunt, K. L. C. 2009, *JChPh*, **130**, 164314
 Harris, W. E. 1996, *AJ*, **112**, 1487
 Helmi, A. 2008, *A&ARv*, **15**, 145
 Hunter, J. D. 2007, *CSE*, **9**, 90
 Ivezić, Ž., Beers, T. C., & Jurić, M. 2012, *ARA&A*, **50**, 251
 Kalirai, J. 2018, *ConPh*, **59**, 251
 Kruijssen, J. M. D. 2014, *CQGr*, **31**, 244006
 Layden, A. C., & Sarajedini, A. 2003, *AJ*, **125**, 208
 Leaman, R., VandenBerg, D. A., & Mendel, J. T. 2013, *MNRAS*, **436**, 122
 Mackey, A. D., & Gilmore, G. F. 2004, *MNRAS*, **355**, 504
 Marchetti, E., Brast, R., Delabre, B., et al. 2007, *Msngr*, **129**, 8
 Marín-Franch, A., Aparicio, A., Piotto, G., et al. 2009, *ApJ*, **694**, 1498
 Massari, D., Fiorentino, G., McConnachie, A., et al. 2016, *A&A*, **586**, A51
 McGregor, P., Hart, J., Stevanovic, D., et al. 2004, *Proc. SPIE*, **5492**, 1033
 McWilliam, A., Geisler, D., & Rich, R. M. 1992, *PASP*, **104**, 1193
 Milone, A. P., Bedin, L. R., Piotto, G., et al. 2008, *ApJ*, **673**, 241
 Milone, A. P., Marino, A. F., Dotter, A., et al. 2014, *ApJ*, **785**, 21

- Milone, A. P., Piotto, G., Bedin, L. R., et al. 2012a, *A&A*, **540**, A16
- Milone, A. P., Piotto, G., Bedin, L. R., et al. 2012b, *ApJ*, **744**, 1
- Monelli, M., Testa, V., Bono, G., et al. 2015, *ApJ*, **812**, 25
- Moretti, A., Piotto, G., Arcidiacono, C., et al. 2009, *A&A*, **493**, 539
- Muñoz, C., Geisler, D., & Villanova, S. 2013, *MNRAS*, **433**, 2006
- Neichel, B., Lu, J. R., Rigaut, F., et al. 2014a, *MNRAS*, **445**, 500
- Neichel, B., Rigaut, F., Vidal, F., et al. 2014b, *MNRAS*, **440**, 1002
- O'Malley, E. M., Gilligan, C., & Chaboyer, B. 2017, *ApJ*, **838**, 162
- Pasquato, M., Trenti, M., De Marchi, G., et al. 2009, *ApJ*, **699**, 1511
- Piersimoni, A. M., Bono, G., & Ripepi, V. 2002, *AJ*, **124**, 3
- Pietrinferni, A., Cassisi, S., Salaris, M., & Castelli, F. 2004, *ApJ*, **612**, 168
- Piotto, G., Milone, A. P., Bedin, L. R., et al. 2015, *AJ*, **149**, 91
- Renzini, A. 2013, *MmSAI*, **84**, 162
- Renzini, A. 2017, *MNRAS*, **469**, L63
- Renzini, A., D'Antona, F., Cassisi, S., et al. 2015, *MNRAS*, **454**, 4197
- Richard, C., Gordon, I. E., Rothman, L. S., et al. 2012, *JQSRT*, **113**, 1276
- Rigaut, F., Neichel, B., Boccas, M., et al. 2014, *MNRAS*, **437**, 2361
- Roediger, J. C., Courteau, S., Graves, G., et al. 2014, *ApJS*, **210**, 1
- Saracino, S., Dalessandro, E., Ferraro, F. R., et al. 2015, *ApJ*, **806**, 152
- Saracino, S., Dalessandro, E., Ferraro, F. R., et al. 2016, *ApJ*, **832**, 48
- Saracino, S., Dalessandro, E., Ferraro, F. R., et al. 2018, *ApJ*, **860**, 95
- Sarajedini, A., Bedin, L. R., Chaboyer, B., et al. 2007, *AJ*, **133**, 1658
- Saumon, D., & Marley, M. S. 2008, *ApJ*, **689**, 1327
- Schirmer, M. 2013, *ApJS*, **209**, 21
- Schirmer, M., Carrasco, E. R., Pessev, P., et al. 2015, *ApJS*, **217**, 33
- Searle, L., & Zinn, R. 1978, *ApJ*, **225**, 357
- Simunovic, M., & Puzia, T. H. 2016, *MNRAS*, **462**, 3401
- Skrutskie, M. F., Cutri, R. M., Stiening, R., et al. 2006, *AJ*, **131**, 1163
- Soto, M., Bellini, A., Anderson, J., et al. 2017, *AJ*, **153**, 19
- Stetson, P. B. 1987, *PASP*, **99**, 191
- Stetson, P. B. 1994, *PASP*, **106**, 250
- Tamai, R., Koehler, B., Cirasuolo, M., et al. 2018, *Proc. SPIE*, **10700**, 1070014
- Turri, P., McConnachie, A. W., Stetson, P. B., et al. 2015, *ApJL*, **811**, L15
- Turri, P., McConnachie, A. W., Stetson, P. B., et al. 2017, *AJ*, **153**, 199
- VandenBerg, D. A., Bergbusch, P. A., Ferguson, J. W., & Edvardsson, B. 2014, *ApJ*, **794**, 72
- Van Der Walt, S., Colbert, S. C., & Varoquaux, G. 2011, *MCSE*, **13**, 22
- Vanzella, E., Calura, F., Meneghetti, M., et al. 2017, *MNRAS*, **467**, 4304
- Wagner-Kaiser, R., Sarajedini, A., von Hippel, T., et al. 2017, *MNRAS*, **468**, 1038
- Wagner-Kaiser, R., Stenning, D. C., Sarajedini, A., et al. 2016, *MNRAS*, **463**, 3768
- Watson, F. G., Hook, I. M., & Colless, M. M. 2006, in *Astrophysics Update 2*, ed. J. Mason (Chichester: Praxis), 363